Petroleum Science 19 (2022) 2027–2045

Contents lists available at ScienceDirect

Petroleum Science

journal homepage: www.keaipublishing.com/en/journals/petroleum-science

Original Paper

# Automatic microseismic events detection using morphological multiscale top-hat transformation

Guo-Jun Shang [a], Wei-Lin Huang [a, *], Li-Kun Yuan [b], Jin-Song Shen [a], Fei Gao [a], Li-Song Zhao [c]

[a] State Key Laboratory of Petroleum Resources and Prospecting, China University of Petroleum—Beijing, Beijing, 102249, China
[b] Department of Automation, China University of Petroleum—Beijing, Beijing, 102249, China
[c] Hebei Coal Research Institute Company Ltd., Jizhong Energy Group, Xingtai, Hebei 054000, China

ARTICLE INFO

*Article history:*
Received 19 August 2021
Received in revised form
8 June 2022
Accepted 8 August 2022
Available online 13 August 2022

Edited by Jie Hao

*Keywords:*
Microseismic events detection
Multiscale morphology
Top-hat transformation

ABSTRACT

The occurrence of microseismic is not random but is related to the physical properties of the underground medium. Due to the low intensity and the influence of noise, microseismic eventually lead to poor signal-to-noise ratio. We proposed a method for automatic detection of microseismic events by adoption of multiscale top-hat transformation. The method is based on the difference between the signal and noise in the multiscale top-hat transform section and achieves the detection on a specific section. The microseismic data are decomposed into different scales by multiscale morphology top-hat transformation firstly. Then the potential microseismic events could be detected by picking up the peak value in the multiscale top-hat section, and the characteristic profile obtains the start point with a specific threshold value. Finally, the synthetic data experiences demonstrate the advantages of this method under strong and weak noisy conditions, and the filed data example also shows its reliability and adaptability.



## 1. Introduction

With the continuous development of social economy, the demand for energy is increasing day by day. In addition to conventional energy sources such as coal, oil, and natural gas, unconventional oil and gas have attracted more and more attention, and shale oil and gas is regarded as an important part of unconventional oil and gas (Hu et al., 2021). Hydraulic fracturing is a widely used conventional oil and gas well stimulation technology and is one of the key technologies for shale gas reservoir exploitation (Dong et al., 2020). Microseismic monitoring is a technique used to image the volume of rock stimulated by hydraulic fracturing (Albright and Pearson, 1982) and has been extensively applied to many fields such as oil and gas reservoir dynamic monitoring, shale gas reservoir exploitation and coal mining (Phillips et al., 1998; Rutledge et al., 2004; Baig and Urbancic, 2010; Maxwell et al., 2010). For the research of microseismic monitoring, how to detect events efficiently and accurately is always an interesting topic, especially the automatic detection methods, which determines the accuracy of subsequent processing and interpretation.

Many researchers have made great efforts in the research of automatic detection methods. A big step towards automatic detection is the proposal of STA/LTA method which select two windows with different lengths to calculate the energy of the data in the two windows respectively and regard the point with the largest energy ratio as the first break time (Allen, 1982; Liu and Zhang, 2014; Zhang et al., 2017). Higher-order statistics are used to weak signals detection due to their excellent performance in removing Gaussian noise and their particularly significant response to signal abrupt changes (Yung and Ikelle, 1997; Saragiotis et al., 2002; Kuperkoch et al., 2010). Cross correlation method as a signal detection method that has been widely used for a long time. It can effectively detect the unknown signal by cross correlating the input data and the template waveform (Molyneux and Schmitt, 1999; Gibbons and Ringdal, 2010; De Meersman et al., 2009; Akram and Eaton, 2016; Tan and He, 2016; Yu et al., 2019). The continuous wavelet transform can restore the maximum amplitude waveform of the first arrival wave, at the same time, highlight the break point time of first arrival to improve the accuracy of picking

* Corresponding author.
*E-mail address:* cup_hwl@126.com (W.-L. Huang).

https://doi.org/10.1016/j.petsci.2022.08.005

first arrival (Zhang et al., 2003; Mousavi and Langston, 2016; Mousavi et al., 2016; Wang et al., 2020). Envelope functions can produce an outline of the seismogram where every point on the outline is greater than or equal to zero. An envelope function can reduce the meaningless LTAs and STAs due to positive and negative amplitudes and improve the automatic picking (Gou et al., 2011; Hafez et al., 2013; Long et al., 2020). Akaike information criterion (AIC) method considers that the signal and noise in the microseismic data have different statistical characteristics, and when the two signals are fitted, the place with the smallest fitting value is regarded as the initial arrival time of the microseismic signal (Leonard, 2010; Diehl et al., 2009; Liu et al., 2017). The empirical mode decomposition (EMD)-based pickers can not only suppress the noise while retaining the original signal features to the greatest extent, but also highlight and enhance the first-arrival information features, thereby improving the picking accuracy (Kirbas and Peker, 2018). In recent years, more and more machine learning algorithms have also been used for weak signal detection (McCormack et al., 1993; Muller et al., 1998; Provost et al., 2017; Rouet-Leduc et al., 2017; Shahnas et al., 2018; Huang, 2019; Zhou et al., 2020; Zhang et al., 2021; Yuan et al., 2022).

The energy ratio based algorithms were more efficient in terms of computational speed compared with other algorithms and can provide reasonably accurate and precise arrival picks. The STA/LTA technique remains one of the most popular methods because of its simple principle, and generally performs well for mildly or moderately noisy data. However, the STA/LTA method shows great inadaptability in some cases of low SNR. If that ratio is higher than a threshold value, the arrival of an event is declared, and a corresponding arrival time is calculated. But it is hard to set some parameters to avoid false triggers if the ratio is lower than the threshold value (Trnkoczy, 2012). Hence, algorithm's performance under the low SNR condition is the focus of research.

As a signal-processing methodology, mathematical morphology (Matheron, 1975) has been applied successfully to many fields, such as vision detection (Haralick et al., 1987; Vincent, 1993), computer vision (Peng et al, 2010), and medical image analysis (Mukhopadhyay and Chanda, 2000, 2002). It was first introduced into seismic data processing for suppressing noise as mathematical morphological filtering (Zheng and Wang, 2003; Li et al., 2005; Wang et al., 2005), unlike other denoising methods, it does not damage the signal components. Multiscale morphology is a commonly used method in mathematical morphology. It can decompose the signal into corresponding scales for related analysis and processing according to the characteristics of the signal on different morphological scales. It was introduced into seismic data processing and has commendable results on noise attenuation (Wang et al., 2008; Duan and Wang, 2010). Recently, morphology and multiscale morphology has been widely used in seismic energy dispersion compensation (Yu et al., 2014), the microseismic denoising (Li et al., 2016), microseismic weak signal detection (Huang et al., 2017a; Shang et al., 2019, 2020; Jiang et al., 2020), fracture-vug identification and extraction (Li et al., 2019) and seismic image interpolation (Huang and Liu, 2020).

Here, a new method is proposed for microseismic signal detection based on multiscale top-hat transformation section which is one type of mathematical morphological algorithm. The proposed method is applied on both synthetic and field examples. In addition, the performances between this approach, AIC method and STA/LTA method are compared, and the results show its superiority to conventional approaches especially under the low SNR conditions. The advantages and disadvantages of the proposed method also be discussed.

## 2. Detection method

### 2.1. Mathematical morphology

Mathematical morphology realizes the computation process by performing operations between the signal and the structural elements (SEs). A SE is a set of elements that can be shifted across the signal. Dilation and erosion are the two basic operations in mathematical morphology theory. These two operations make up different complex subsequent operations through certain permutations and combinations to achieve different functions. The one-dimensional gray dilation and erosion are expressed as follows (Huang et al., 2017b):

$$(f \oplus b)(z) = \max\{f(z-x) + b(x) : \ x \in B\} \tag{1}$$

$$(f \Theta b)(z) = \min\{f(z+x) - b(x) : x \in B\} \tag{2}$$

where $\oplus$ is the dilation operation, $\Theta$ is the erosion operation, $f(x)$ is the signal, $b(x)$ is the elements in SE, $B$ is the number SE set.

Opening and closing are the two operations formed by the combination of dilation and erosion: the operation that erosion followed by dilation is the opening, and the operation that dilation followed by erosion is the closing. These two operations are defined as follows (Serra, 1982):

$$f \circ B = f\Theta B \oplus B \tag{3}$$

$$f \bullet B = f \oplus B \Theta B \tag{4}$$

where o is the opening operation, $\bullet$ is the closing operation, $\oplus$ is the dilation operation and $\Theta$ is the erosion operation. Fig. 1 shows the results of four basic morphological operations using an elliptical SE on a Ricker wavelet signal. The result of dilation operation is always above the original signal, while erosion result is always below the original signal. Most of the opening and closing results are consistent with the input wavelet, except for the peak in opening and trough in closing outputs. This phenomenon indicates

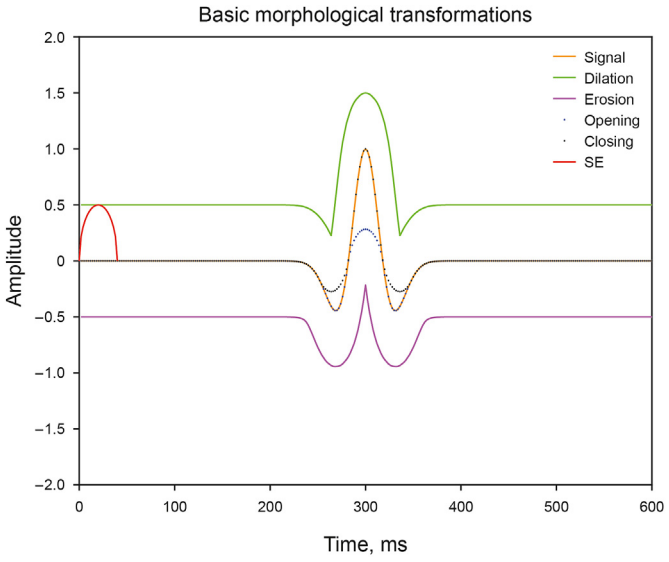


**Fig. 1.** Schematic diagram of the four basic operations of mathematical morphology. The yellow solid line is signal, the red semi-ellipse is the SE. The green solid line is dilation result, the magenta solid line is erosion result, the blue point line is the opening result, and the black point line is the closing result.

that the opening operation can be used to eliminate the sharp peaks, and the closing operation can eliminate the sharp troughs.

### 2.2. Multiscale top-hat transformation

According to the experiences in the field of image processing, morphological top-hat transformation is very practical for extracting tiny shapes and details from the original image. The detection of weak signals is realized by take this advantage. The top-hat transformation contains two types of operations: the white top-hat transformation, and the black top-hat transformation. They are defined as (Serra, 1982):

$$W\_Hat(f) = f - (f \circ B) \tag{5}$$

$$B\_Hat(f) = (f \bullet B) - f \tag{6}$$

where $W\_Hat$ is the result of white top-hat transformation, $B\_Hat$ is the result of black top-hat transformation. $f$ is the input signal, $B$ is the SE, $\circ$ is the opening operation and $\bullet$ is the closing operation. Fig. 2 and Fig. 3 is the diagram of two types of top-hat

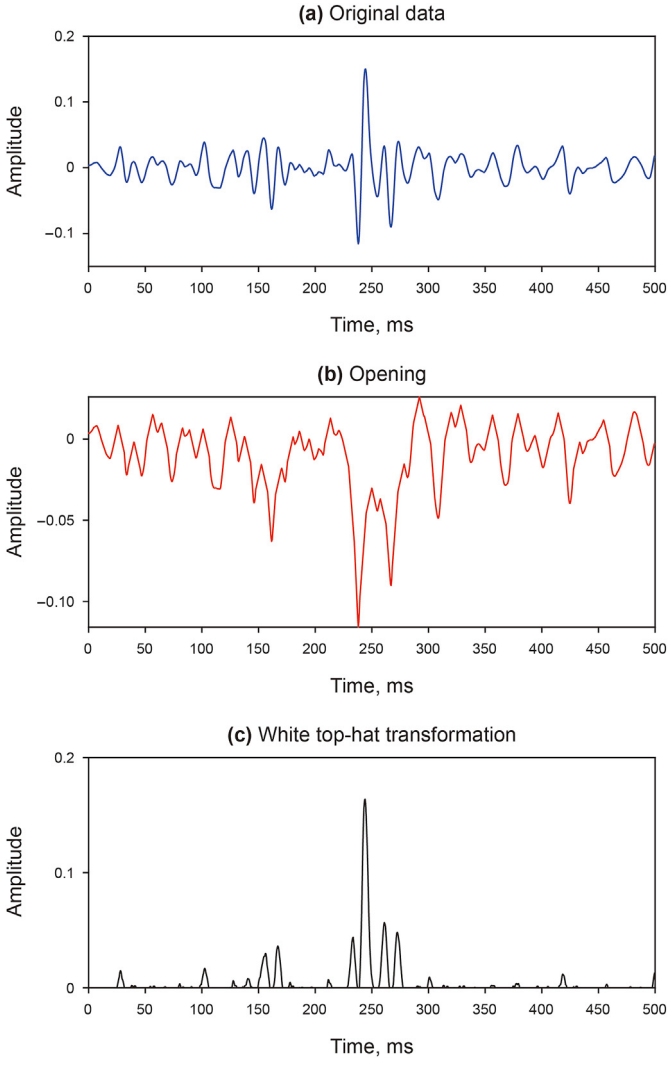


**Fig. 2.** Diagram of white top-hat transformation, where (a) is the original data, (b) is the opening result, and (c) is the white top-hat transformation result. The length of SE is 181.

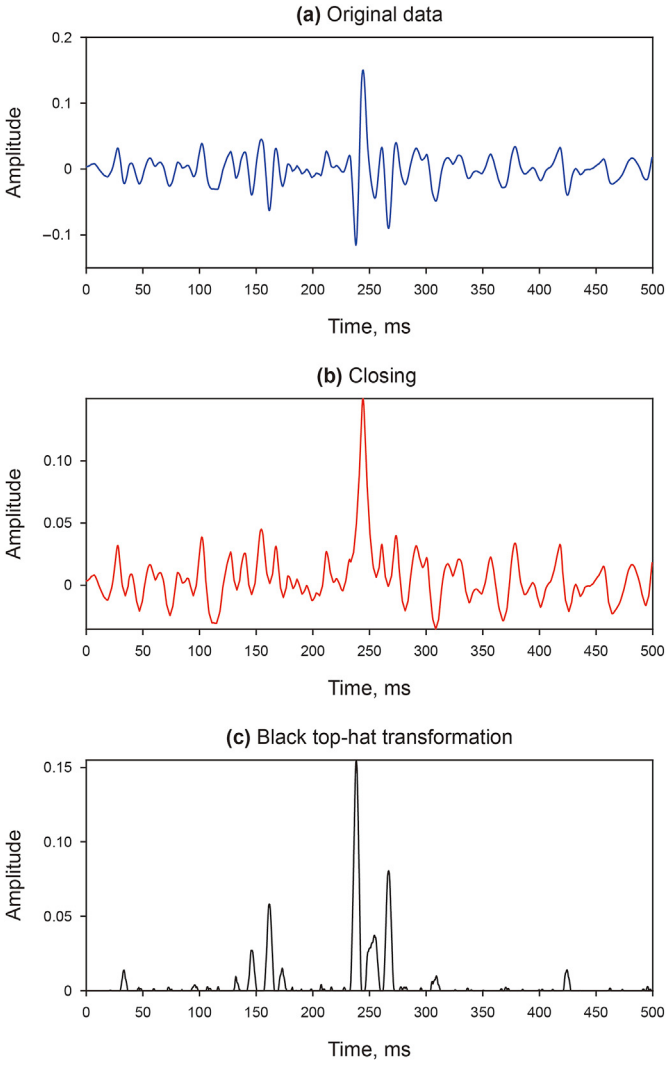


**Fig. 3.** Diagram of black top-hat transformation, where (a) is the original data, (b) is the closing result, and (c) is the black top-hat transformation result. The length of SE is 181.

transformations. The results of both two transformations are nonnegative. The white top-hat transformation can be used for detecting the peak, while the black top-hat transformation can be used for detecting the trough. With the length of the SE is bigger than the signal, top-hat transformations can extract all the peak and trough waveforms in the signal.

The top-hat transformation section of the signal is gotten (Mukhopadhyay and Chanda, 2001, 2002) by:

$$Top\_Hat(f) = \frac{W\_Hat(f) + B\_Hat(f)}{2} \tag{7}$$

Fig. 4 shows the input data (blue line) and its top-hat transformation section. Based on prior information, the black part in Fig. 4a are microseismic signals need to be detected, and its start is the first break (the red star). The position of the maximum value of the top-hat transformation section in Fig. 4b corresponds to position of the maximum value of the microseismic signal in Fig. 4a. The starting point (the bule star) of the black part in Fig. 4b, that is, the position of the first non-zero point corresponds to the position of the red star in Fig. 4a. This provides an idea for detecting the

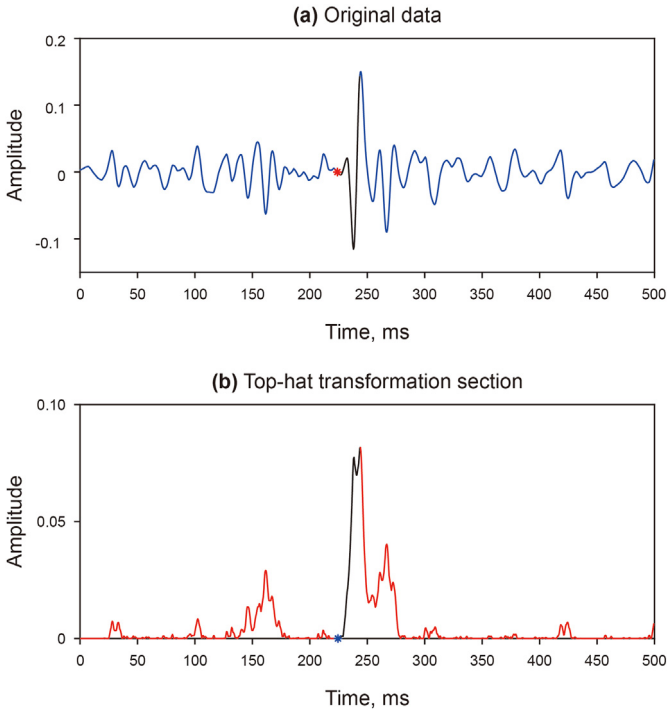


**Fig. 4.** Diagram of microseismic signal detection by top-hat transformation. (a) is the original data, (b) is the top-hat transformation section. The black parts in (a) are microseismic signals of the original data, and the black parts in (b) corresponding to the black parts in (a). The length of SE is 181.

microseismic signal, that is, firstly by finding the position of the maximum value of the top-hat transformation section to determine the position of the maximum absolute value amplitude of the microseismic signal, and then using the first non-zero point before the maximum value in the top-hat transformation section to determine the first break.

Figs. 5, 6 and 7 demonstrate the influence of SE type, SEs' height, and SEs' length on the top-hat transformation section. The same original data as in Fig. 4 was used in these two picture, and based on prior information, the black part in Fig. 5a, Fig. 6a and Fig. 7a are from the first break to the maximum amplitude point of the microseismic signal. The black part in Fig. 5b to Fig. 5d show that the top-hat transformation sections obtained using elliptical SEs are the best for microseismic signal detection. The black part in Fig. 6b to Fig. 6d show that the top-hat transformation section obtained using the SEs with a height slightly greater than the original signal maximum are the best for microseismic signal detection. The black part in Fig. 7b to Fig. 7d show that the top-hat transformation section obtained using the SEs with a length slightly greater than the original signal maximum are the best for microseismic signal detection.

In microseismic data processing, the received signal usually contains different scales of signals. Hence, only one scale SE is difficult to achieve the ideal processing effect. In this respect, a multi-scale version of top-hat transformation is developed for weak signal detection. The multiscale opening and closing operation are defined as follows (Matheron, 1975):

$$f \circ B_n = f\Theta B_n \oplus B_n \tag{8}$$

$$f \bullet B_n = f \oplus B_n \Theta B_n \tag{9}$$

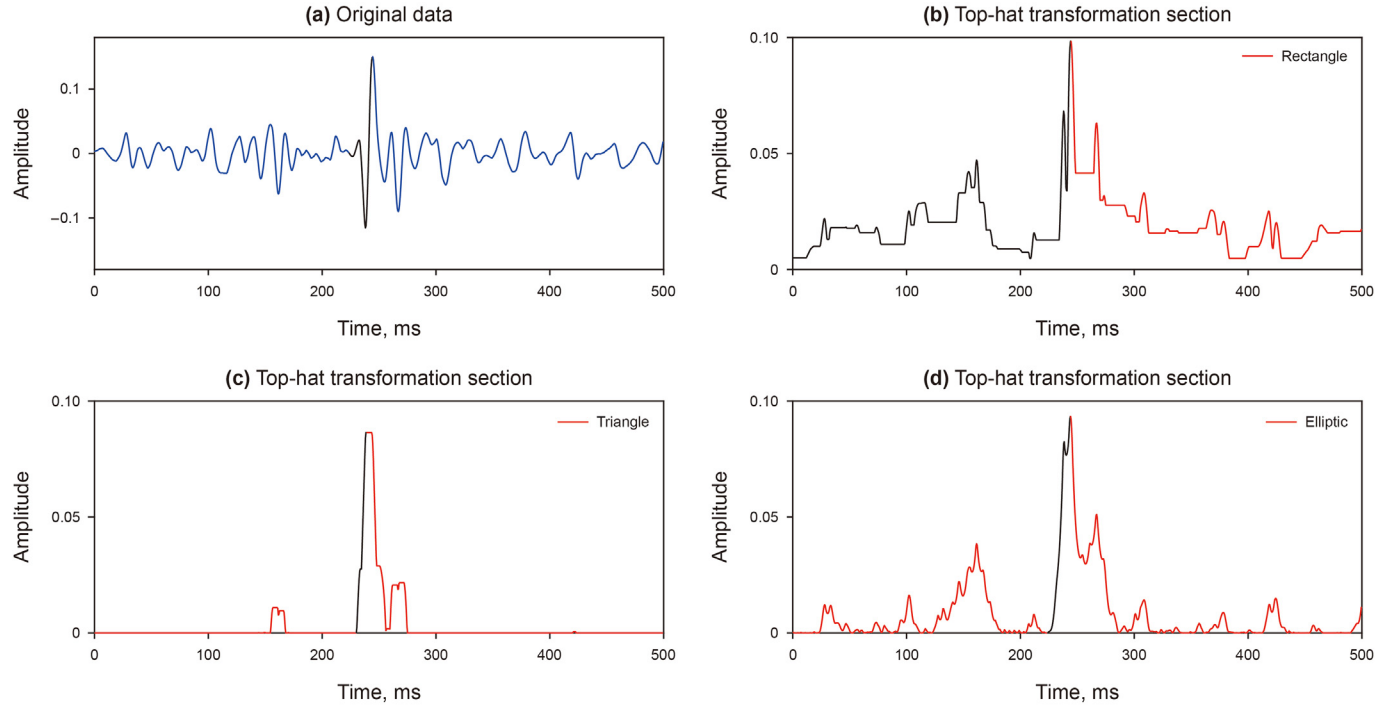


**Fig. 5.** Comparison of top-hat transformation section under different types of SEs. (a) is the original data, the black part is from the first break to the amplitude maximum point. (b) to (d) are top-hat transformation sections obtained using rectangular, triangular, and elliptical SEs, respectively. All types of SEs have a height of 0.2 and a length of 49 samples. The black part in (b) is from the start point of top-hat transformation section to the maximum value point. The black part in (c) and (d) are from the first non-zero point before the maximum value point to the maximum value point.

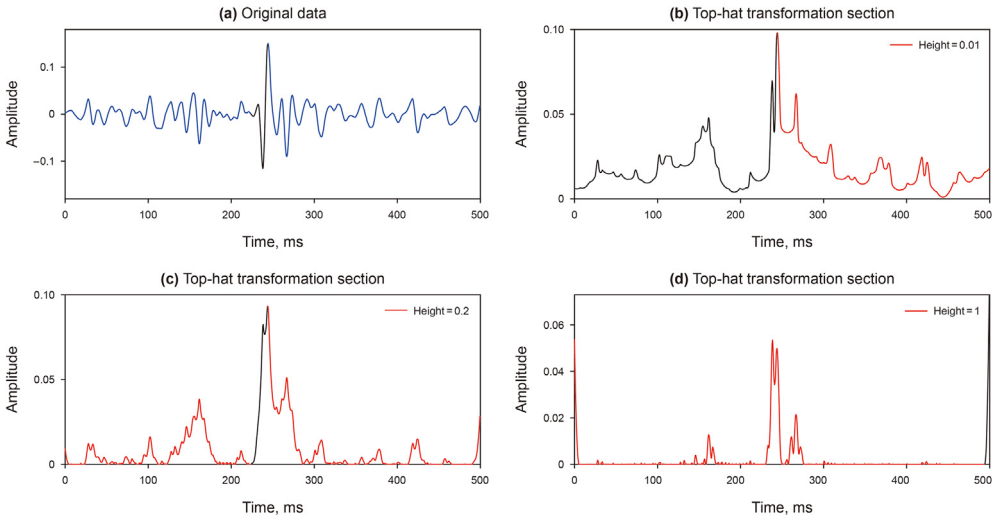


**Fig. 6.** Comparison of top-hat transformation section under different heights of SEs. (a) is the original data, the black part is from the first break point to the amplitude maximum point. (b) to (d) are top-hat transformation sections obtained using SEs with heights of 0.01, 0.2, and 1, respectively. All SEs are elliptical SEs and have a length of 49 samples. The black part in (b) is from the start point of top-hat transformation section to the maximum value point. The black part in (c) and (d) are from the first non-zero point before the maximum value point to the maximum value point.

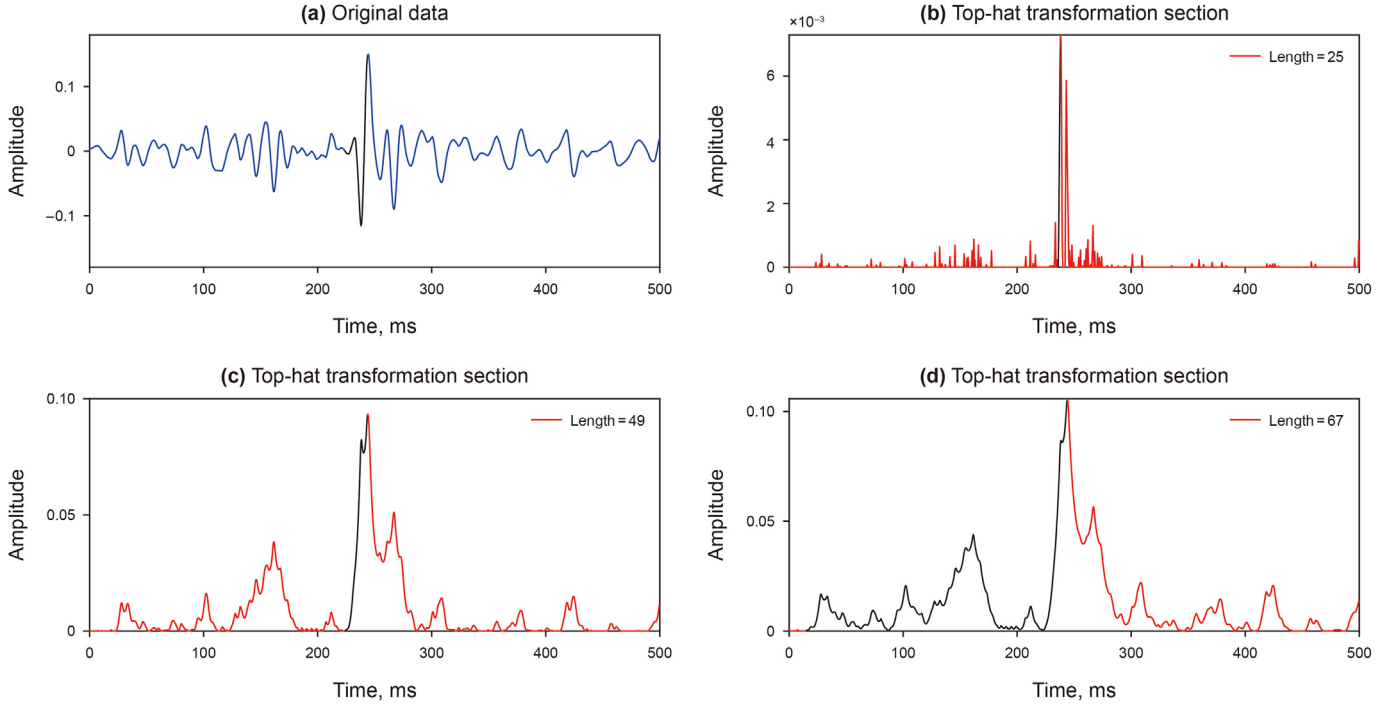


**Fig. 7.** Comparison of top-hat transformation section under different lengths of SEs. (a) is the original data, the black part is from the first break point to the amplitude maximum point. (b) to (d) are top-hat transformation sections obtained using SEs with lengths of 25, 49, and 67 samples, respectively. All SEs are elliptical SEs and have a height of 0.2. The black part in (b) to (d) are from the first non-zero point before the maximum value point to the maximum value point.

where $B_n$ is the $n$th SE. If the initial SE is $B$, $B_n$ can be obtained by dilating the initial $B$ itself for $n$-1 times, and it can be defined as:

$$B_n = B \oplus B \oplus \underbrace{\ldots \oplus B}_{n-1} \quad (10)$$

Fig. 8 is the self-dilation of the three types of common SEs. It indicates that self-dilation does not change the type of SEs, but the length and height of SEs.

Two kinds of multiscale top-hat transformations are defined as follows (Bai et al., 2012):

$$W\_Hat_n(f) = f - (f \circ B_n) \quad (11)$$

$$B\_Hat_n(f) = (f \bullet B_n) - f \quad (12)$$

where $W\_Hat_n$ and $B\_Hat_n$ are multiscale white top-hat transformation and multiscale black top-hat transformation, respectively. The two types of multiscale top-hat transformations are shown in Fig. 9 and Fig. 10.

To better analyze the results of multiscale top-hat

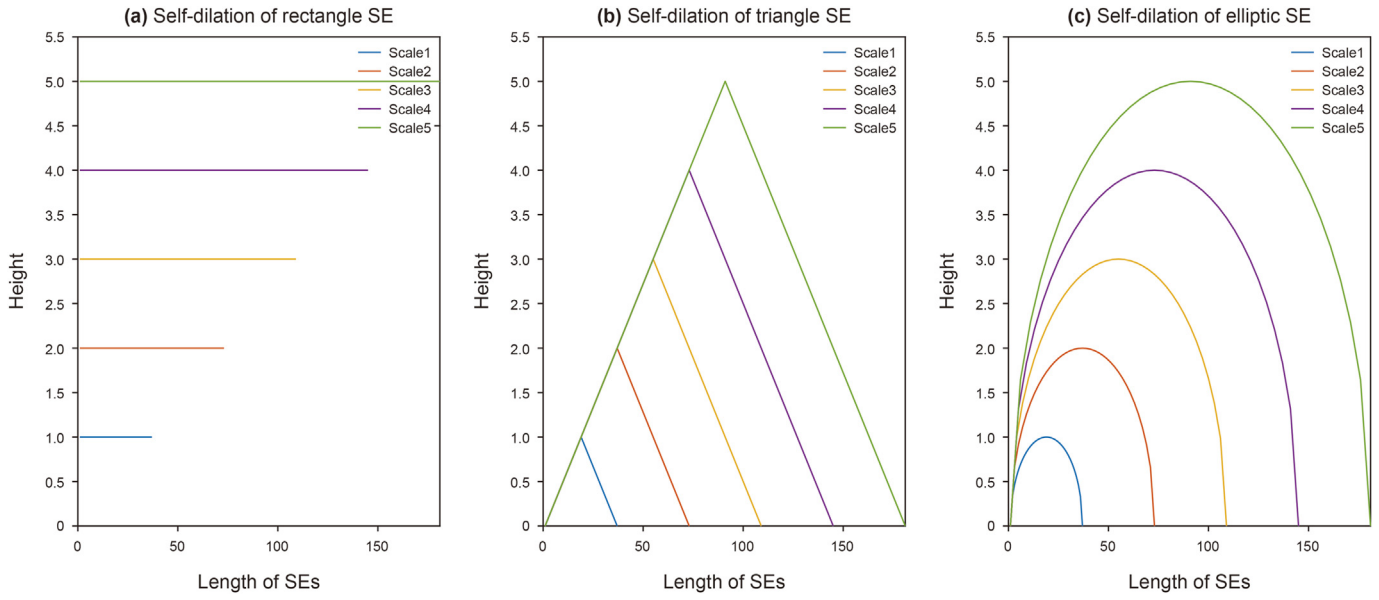


**Fig. 8.** Self-dilation diagram of the three types of common SEs. The three types of SEs are rectangles, triangles, and ellipses. The length of SEs from scale 1 to scale 5 are 37, 73, 109, 145, and 181.

transformation, some amplitude outliers have been added before the black highlighted parts which is the microseismic signal need to be detected, whose values are greater than the peak value of the original data. The results of both multiscale white top-hat transformation and multiscale black top-hat transformation have the same tendency. Take the white multiscale top-hat transform as an example, at the beginning, the results of the white top-hat transformation change significantly with the increase of the length of the SE (like from scale 1 to scale 4), but the results no longer change when the length of the SE increases to a certain length (like from scale 4 to scale 5). Each scale section contains two amplitudes protruding areas corresponding to the added amplitude outlier area and the black part of original data respectively, they are defined as area 1 and area 2 by the order of appearance on the X axis. In scale 1, the ratio of the maximum amplitude of area 1 and area 2 is greater than 1, and the maximum value of the white top-hat transformation is in area 1. With the increase of length of the SE, the ratio decreases gradually. In scale 5, the result of the white top-hat transformation is unchanged, the ratio is less than 1, and the maximum value of this scale is in area 2. The position of the maximum value of the white top-hat transformation coincides with the position of the peak of the microseismic signal. Similarly, the multiscale top-hat transformation section like as Eq. (7) can be gotten:

$$Top - Hat_n(f) = \frac{W\_Hat_n(f) + B\_Hat_n(f)}{2} \tag{13}$$

Fig. 11 is the multiscale top-hat transformation section calculated by Eq. (13) using the results in Figs. 9 and 10. The multiscale top-hat transformation can utilize the differences between noise and signal in different scale SE to separate them in some scale section and continuously highlight the microseismic signal. Just like Fig. 9, the scale 4 and scale 5 sections in Fig. 11 have almost no change, which is reasonable for microseismic signal detection. Scale 4 section contains two amplitudes protruding areas corresponding to the added amplitude outlier area and the black part of original data respectively, and they are defined as area 1 and area 2 by the order of appearance on the X axis. The maximum value of scale 4 section is in the area 2, and its position marked the peak position of microseismic signal. The starting point of area 2, that is, the first non-zero point, is consistent with the first break of the black part in the original data. So, the microseismic signal was detected by finding the maximum value of a certain scale section and the first break was determined by the first non-zero point before the maximum value in the top-hat transformation section.

### 2.3. Signal detection method

The selection of SEs plays an important role in the multiscale top-hat transformation section. In some cases, due to low signal-to-noise ratio (SNR), there is no zero point on the top-hat transformation section and the first break of microseismic signal cannot be detected. A threshold was set manually to make the values of the top-hat transformation section that less than the threshold to 0. Fig. 12 shows the three different top-hat transformation sections under different thresholds. Compared with the first break of black part on Fig. 12a, the starting point of the black part on top-hat transformation section under too small threshold (Fig. 12c) is smaller, and the starting point of the black part on top-hat transformation section under too large threshold (Fig. 12d) is larger, neither of which gives an accurate first break result. The starting point of the black part on top-hat transformation section under suitable threshold (Fig. 12b) coincides with the first break in Fig. 12a which gives an accurate first break result.

The proposed method determines the key parameters such as the length of the initial SE, the number of scales, the scale selected for picking, and the threshold through the template, and uses these key parameters to realize the automatic picking of the first break of all data without human intervention. The details of the proposed method are as follow:

(1) Select a record ($d$) with a relatively high SNR from the microseismic dataset as the template to determine the scale section and threshold.
(2) Choose an appropriate length of initial SE ($b$), number of scales ($N$) and a time window, performing multiscale top-hat

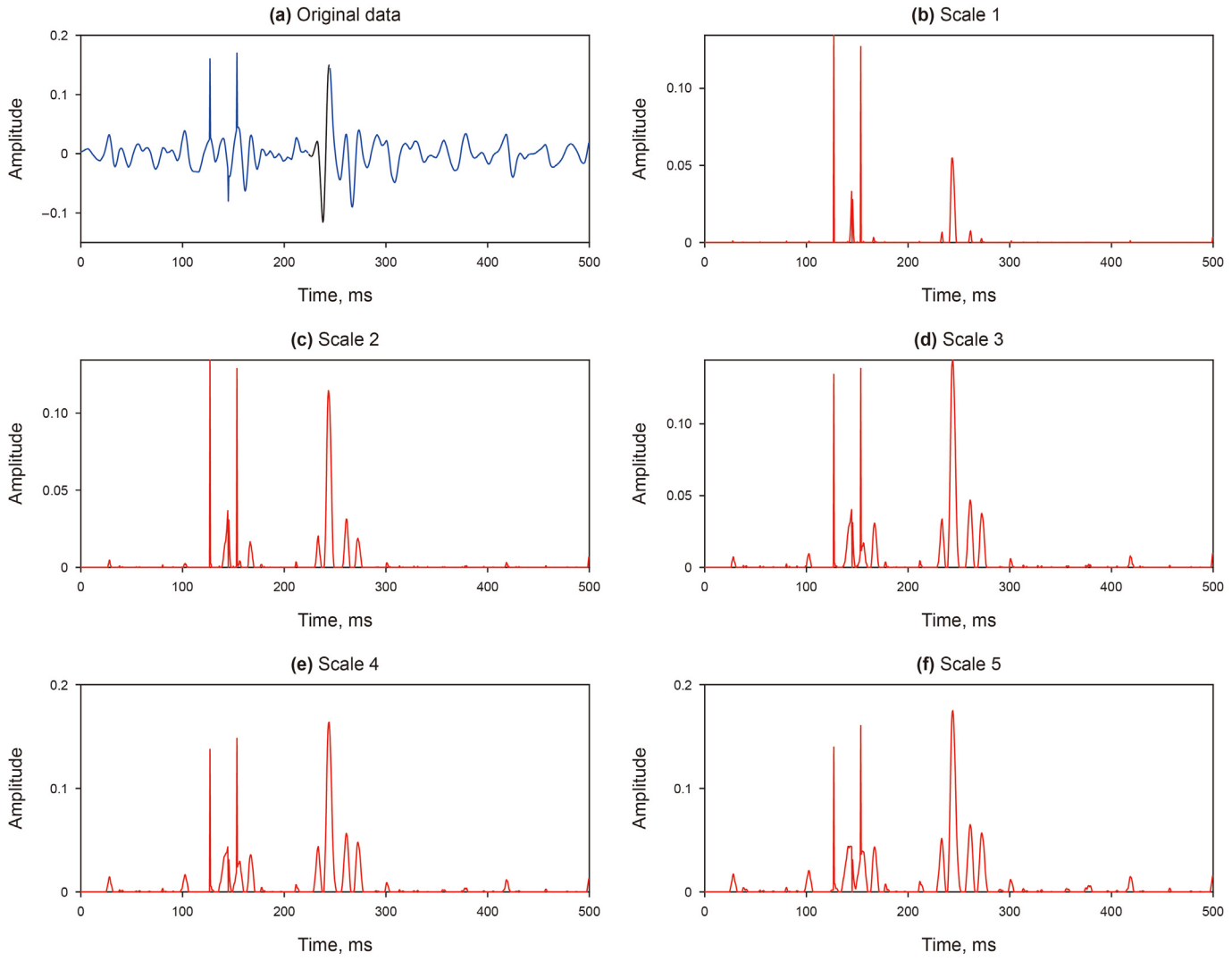


**Fig. 9.** Diagram of multiscale white top-hat transformation, where (a) is original data which black part is microseismic signal, and from (b) to (f) are the results of the multiscale white top-hat transformation at five different scales. The SEs are elliptical SEs and the length of SEs from scale 1 to scale 5 are 37, 73, 109, 145, and 181.

transformation in the selected time window on the template, and getting each scale top-hat transformation section ($S_n$) by Eqs. (8) to (13).

$$S_n(d) = \frac{d \bullet b_n - d \circ b_n}{2}, 1 \le n \le N \tag{14}$$

where $b_n$ represents the SE of $b$ self-dilated $n$-1 times. The length of initial SE usually is an odd number around 10, which can ensure that the length of the SE will not increase too much from the previous scale when it dilates itself. The value of $N$ is determined according to the following rules: the height of the SE after being dilated $N$-1 times is not one order of magnitude higher than the maximum value of $d$.

(3) Normalize all the top-hat transformation section as follows:

$$S'_n(d) = \frac{S_n(d)}{\max(S_n(d))} \tag{15}$$

After normalization, the maximum value on each top-hat transformation section is 1.

(4) Choose a threshold ($\eta$) between 0 and 1 and set all values on top-hat transformation section less than the threshold to 0.

The threshold is related to the smoothness of the signal, and the smoother the signal, the smaller the threshold. It can be adjusted by the detection performance of the template.

(5) Select a top-hat transformation section (the scale number of this section is marked as $m$) for microseismic signal detection. Top-hat transformation sections starting from $m$ no longer change. Firstly find the maximum value of this selected section, then find the first non-zero point before the maximum value as the first break of the microseismic signal.
(6) Apply $m$ and $\eta$ to the microseismic dataset, achieving the automatic microseismic signal detection.

## 3. Synthetic dataset example

To verify the accuracy of the proposed method, three synthetic examples are taken first. The synthetic microseismic data received the signal from 12 three-component geophone in wells. The dataset

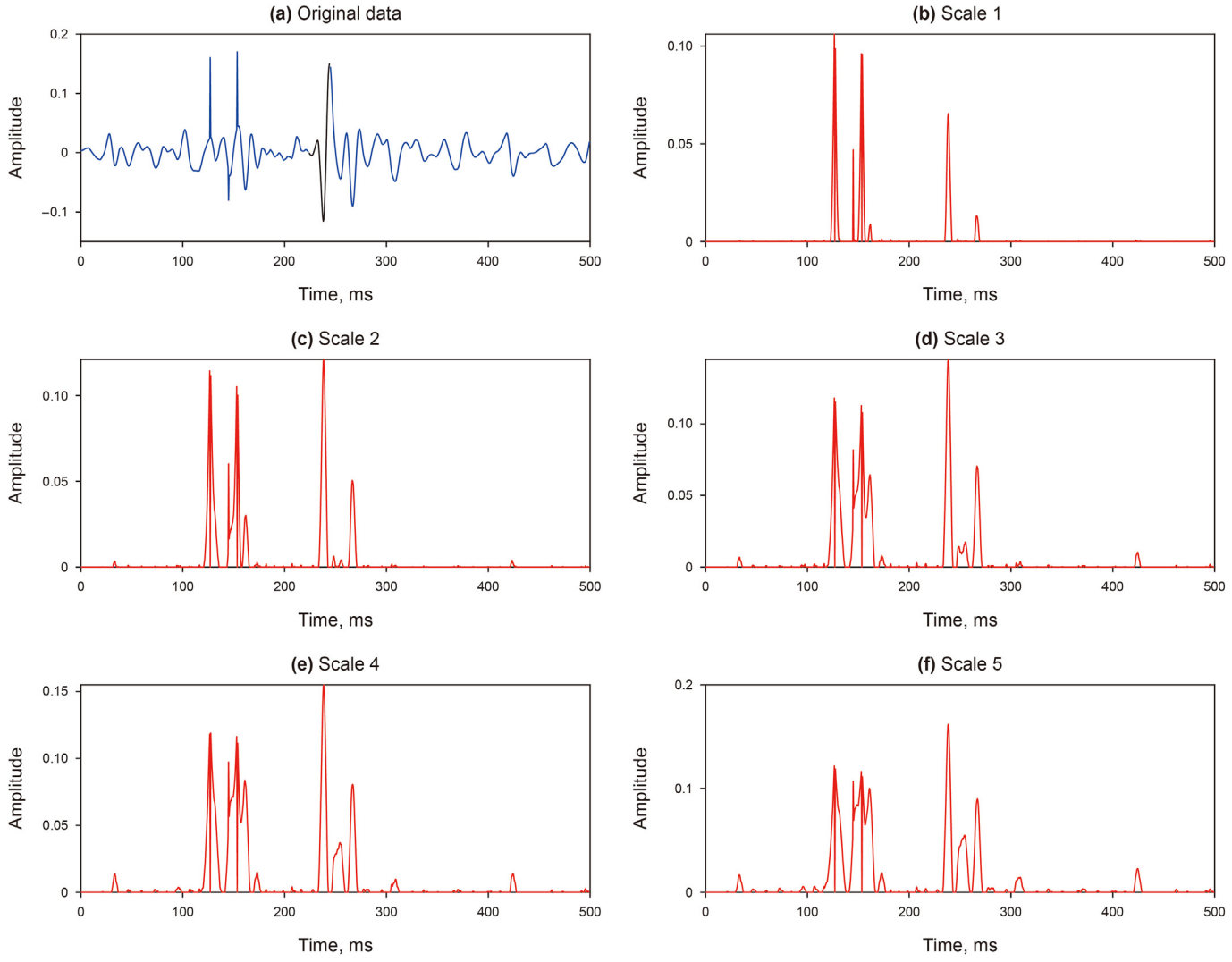


**Fig. 10.** Diagram of multiscale black top-hat transformation, where (a) is original data which black part is microseismic signal, and from (b) to (f) are the results of multiscale black top-hat transformation at five different scales. The SEs are elliptical SEs and the length of SEs from scale 1 to scale 5 are 37, 73, 109, 145, and 181.

has 36 traces, and each trace has the same Ricker wavelet whose dominant frequency is 50 Hz. The time sampling interval is 0.5 ms and the number of time sample is 500. Fig. 13 shows the section of the noise-free synthetic microseismic records.

Meanwhile, the superiority of the proposed method is verified by comparing with the AIC method and the STA/LTA method. Before verifying the performance of the proposed method applied to different synthetic data, the concept of signal-to-noise ratio (SNR) was introduced to measure the quality of the dataset, and it can be calculated as the following formula.

$$\mathrm{SNR} = 10{*}\log_{10}\frac{\sum_{i=1}^{N} signal^2(i)}{\sum_{i=1}^{N} noise^2(i)} \tag{16}$$

where $signal(i)$ and $noise(i)$ represent the signal and noise of microseismic records respectively, $N$ is the length of data. The noise-free data was taken as signal, and then add Gaussian noise with different energies to the noise-free data.

### 3.1. High SNR synthetic dataset

First, the proposed method is tested in a high SNR synthetic data. The SNR is −1 dB and the waveforms are shown in Fig. 14. Although the total energy of the noise in this data is already greater than the total energy of the signal, the signal can be seen easily in Fig. 14. The 5th trace was chosen as the template and the multiscale top-hat transformation section of the trace can be obtained. After research, the length of initial SE is 15, the total number of scales is 10, and the threshold is 0.45. The 10 multiscale top-hat transformation sections after normalized are shown in Fig. 15. The scale sections after scale 5 have little change, and the 6th scale section is chosen for microseismic signal detection. Fig. 16 shows the waveform of 5th trace in both −1 dB and noise-free data and the selected 6th scale section. The waveform of this scale section has a great

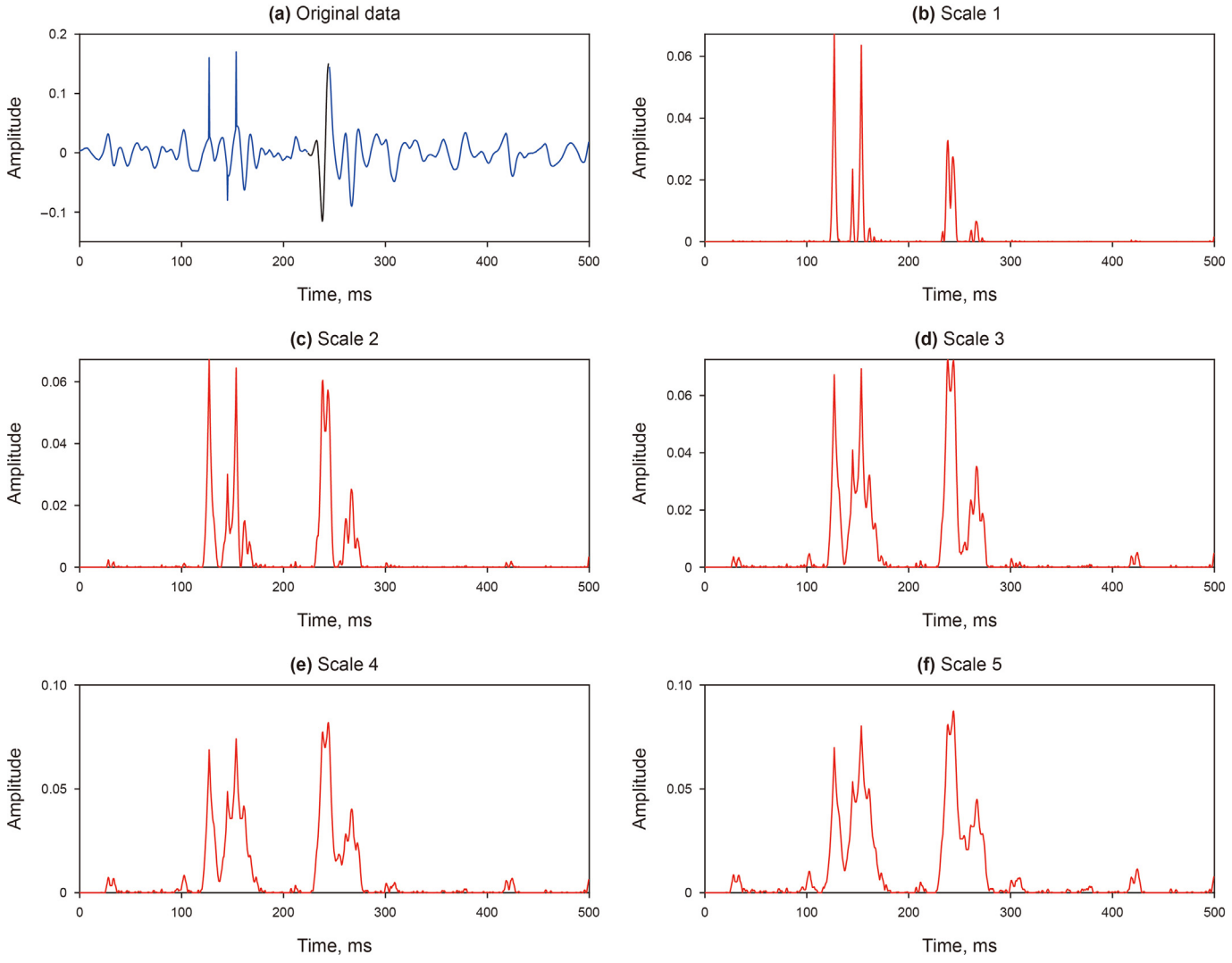


**Fig. 11.** Diagram of multiscale top-hat transformation sections. (a) is original data in which black part is microseismic signal, and from (b) to (f) are the top-hat transformation sections at five different scales. The SEs are elliptical SEs and the length of SEs from scale 1 to scale 5 are 37, 73, 109, 145, and 181.

correlation with the microseismic signal, and its maximum position is the same as that of the microseismic signal, the starting point of the scale section corresponds to the starting point of the microseismic signal. Based on this, the detection of microseismic signal can be achieved.

Next, the detection results of the proposed method are compared with the other two methods. Fig. 17 shows detection results of −1 dB SNR data by the proposed method, AIC method and STA/LTA method. From a macroscopic view, without adjusting the initial setting parameters, it seems that all the three methods have good results.

The detection error is used to numerically evaluate the performance which is defined as follows:

$$E(i) = |(T(i) - \overline{T}) - (t(i) - \overline{t})| * dt \tag{17}$$

where $E(i)$ denotes the detection error for the $i$th trace measured in recordings and its physical unit is ms. $T(i)$ denotes the position corresponding to the exact first arrival for the $i$th trace in a microseismic record and $t(i)$ denotes the identification arrival in samples. $\overline{T}$ and $\overline{t}$ represent the average of $T(i)$ and $t(i)$ , respectively. $dt$ denotes time sampling interval. The exact arrivals are obtained by applying the proposed method to the noise free data. If the $E(i)$ is less than a specific value, the detection of that trace is accurate. Fig. 18 is the histogram of detection errors for the three methods calculated by Eq. (17). It shows that the detection errors of these three methods are all smaller for the −1 dB SNR data, the error threshold is set to 2 ms, and after calculating, the overall detection accuracy of the proposed method and the STA/LTA method is 100%, and the overall detection accuracy of AIC method is 77.78%. For data with high SNR, both the proposed method and STA/LTA method

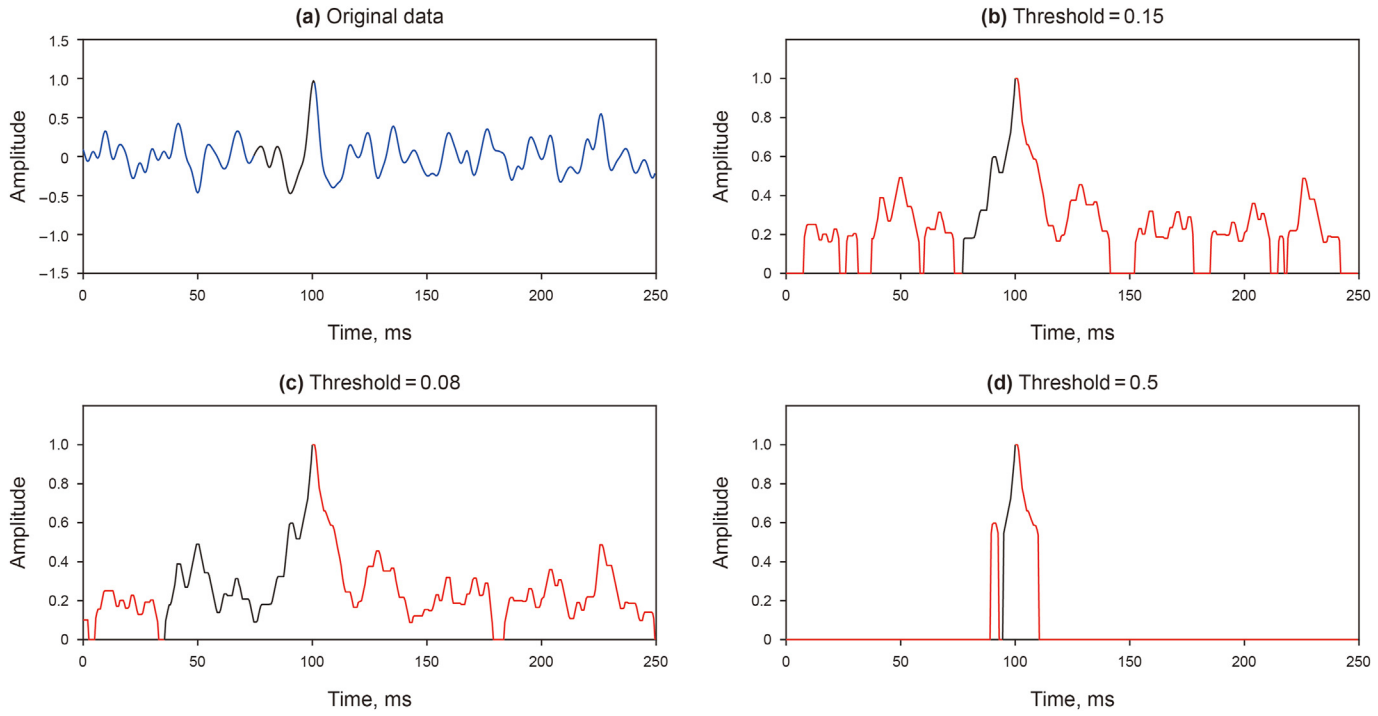


**Fig. 12.** Comparison of the top-hat transformation sections under different threshold conditions. (a) is the original data, where the black part is the first break to the maximum amplitude point. (b) to (d) correspond to the top-hat transformation section under the appropriate, too small, and too large thresholds, respectively, where the start point of the black part is the first non-zero point before the maximum value point, and the end point is the maximum value point.

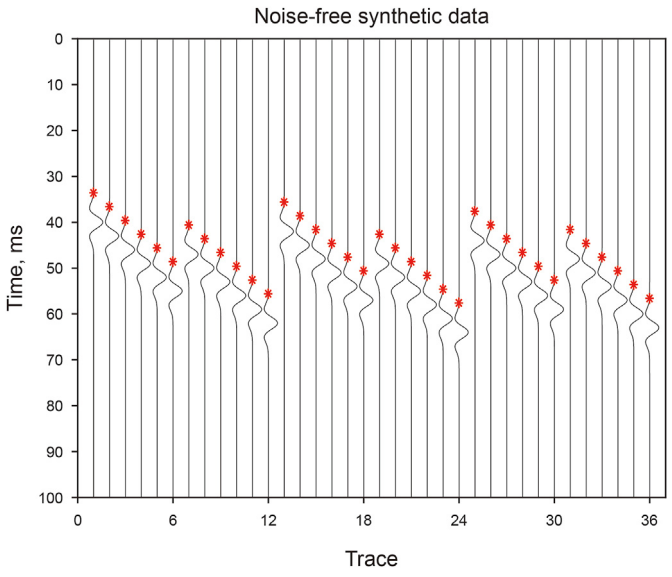


**Fig. 13.** The noise-free synthetic data. The red stars are the first break of microseismic signal.

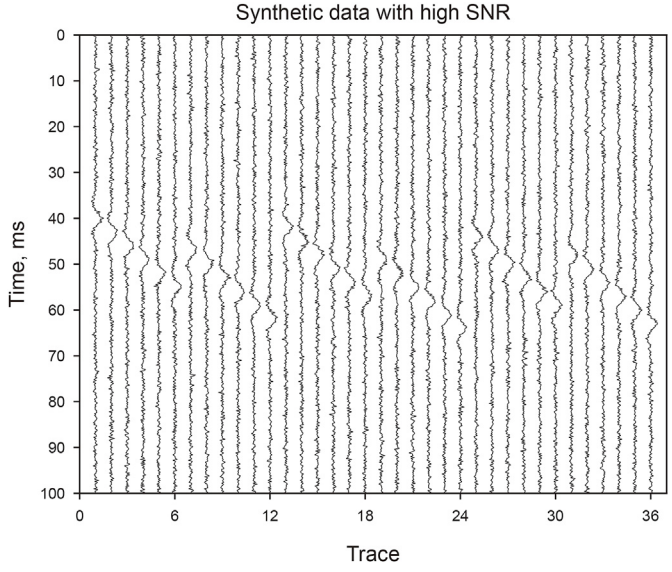


**Fig. 14.** Synthetic data with high SNR. The SNR is −1 dB.

have excellent performance. The cumulative error was used to further compare the performance of the three methods which represents the rule of the total error with the number of traces. Fig. 19 is the cumulative error of the three methods applied to high SNR data. As the number with Y label shows, the proposed method has the smallest cumulative error. The proposed method has the best performance in microseismic events detection of the high SNR data.

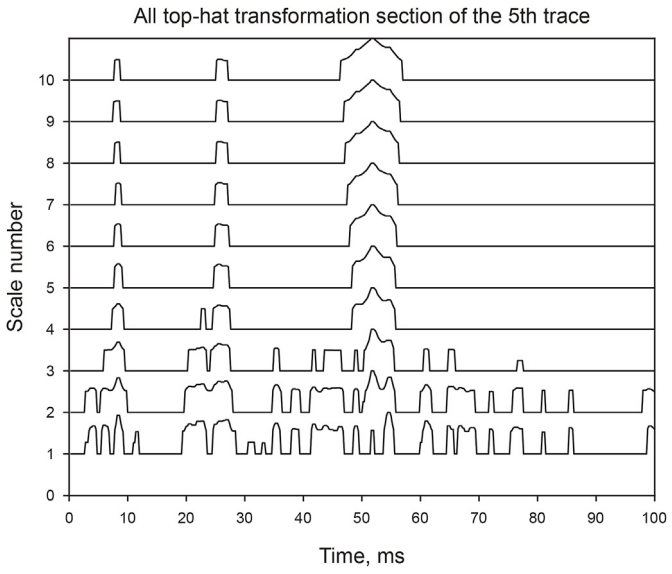


**Fig. 15.** All top-hat transformation sections of the 5th trace of −1 SNR data.

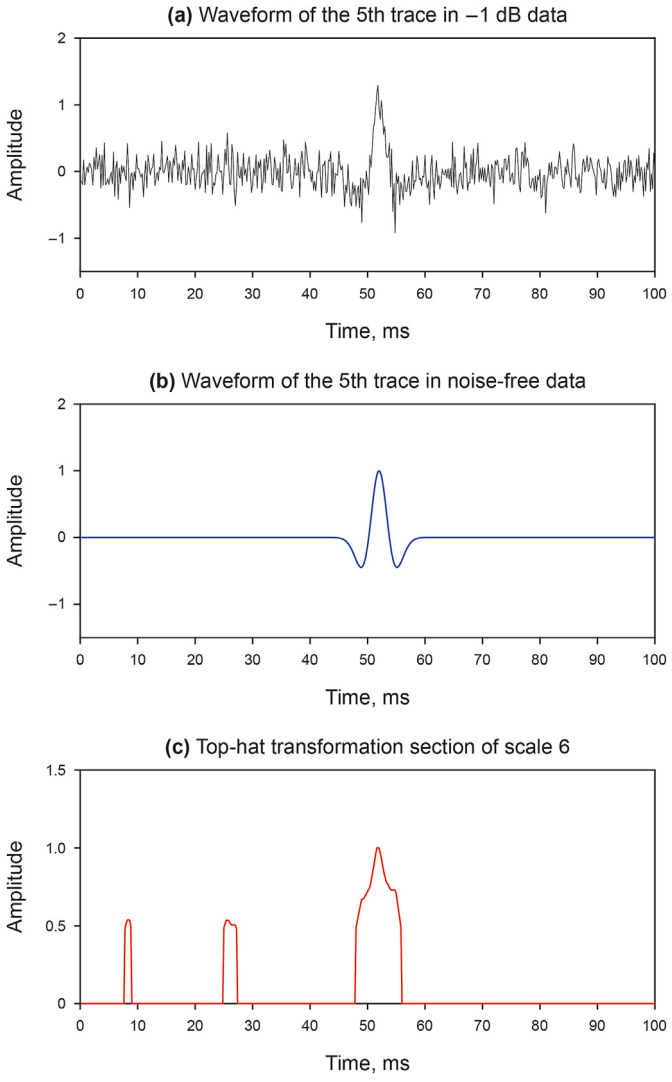


**Fig. 16.** Comparison of waveforms and selected scale section. The black waveform in (a) is the 5th trace in −1 dB data, the bule waveform in (b) is the 5th trace in noise-free data, and red waveform in (c) is the 6th scale section.

### 3.2. Low SNR synthetic dataset

To further illustrate the applicability of the proposed method, these three methods are applied to a low SNR microseismic data. The signal is still the noise-free data in Fig. 13, but the SNR has dropped to −13 dB. It means the noise is much higher than the signal. The waveform is shown in Fig. 20. The signal can hardly see in Fig. 20 due to the low SNR. The traditional methods have difficulty in detection, and it is also a big challenge for the proposed method. The first trace was chosen as the template and the multiscale top-hat transformation section of the trace can be obtained., the length of initial SE is 9, the total number of scales is 10 and the threshold is set to 0.65. The 10 multiscale top-hat transformation sections after normalized are shown in Fig. 21. The scale sections after scale 6 have little change, and the 7th scale section was chosen for microseismic detection. Fig. 22 shows the waveform of 1st trace in both −13 dB and noise-free data and the selected 7th scale section. The waveform of this scale section has a great correlation

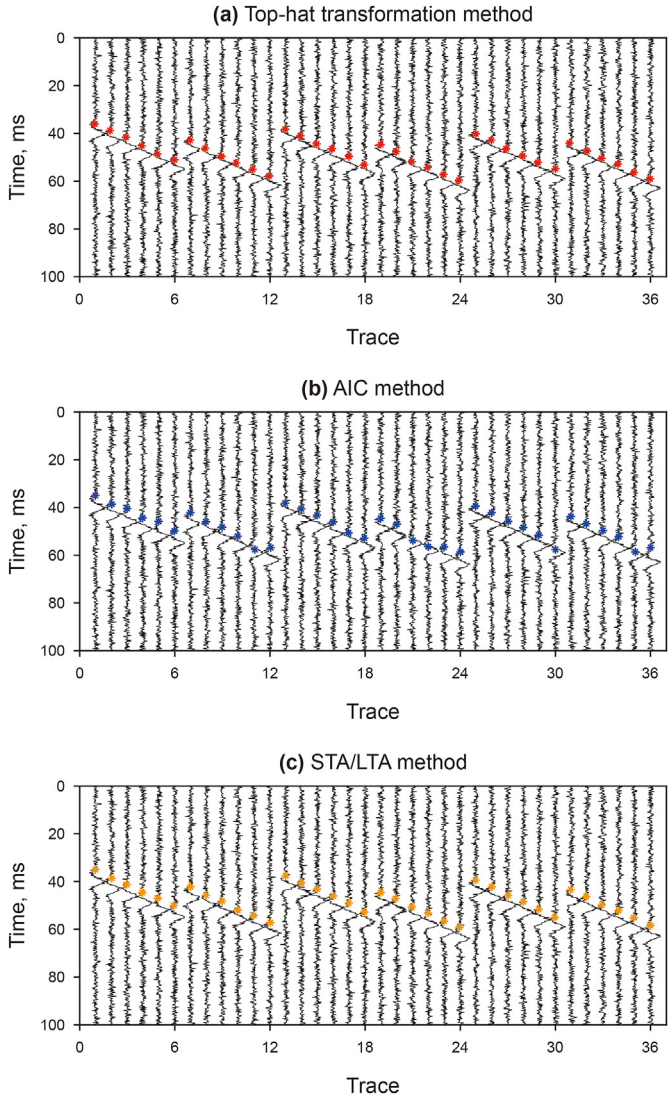


**Fig. 17.** The detection results of −1 dB SNR data using the three methods. The red ones in (a) are the detection results of the proposed method, the blue ones in (b) are the detection results of the AIC method, and the yellow ones in (c) are the detection results of STA/LTA method.

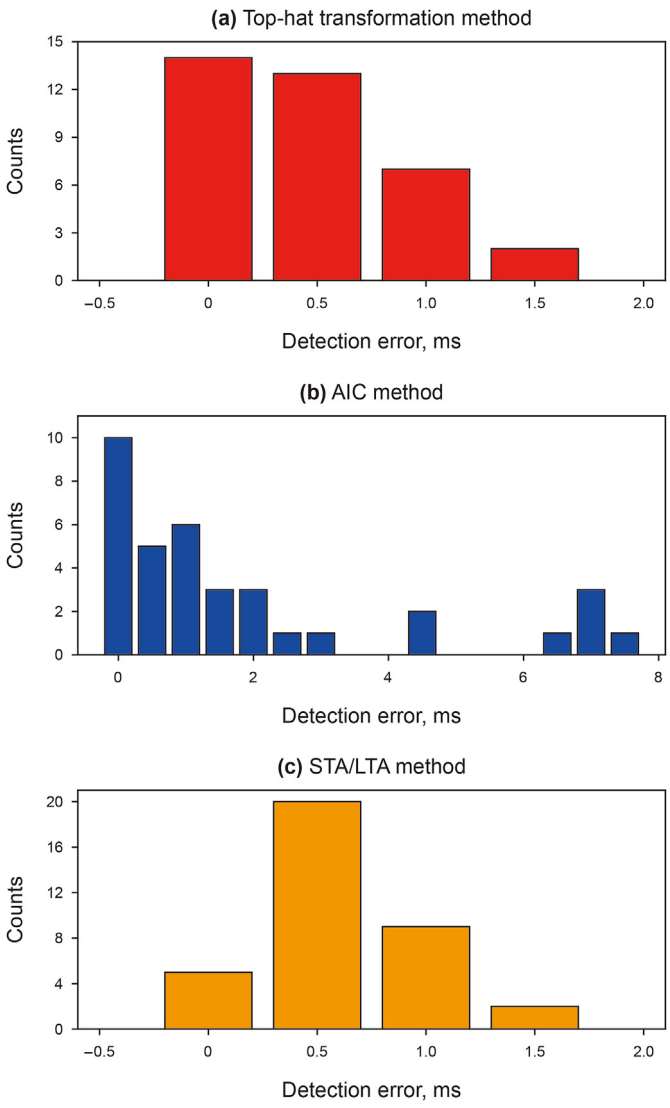


**Fig. 18.** The histogram of detection errors of −1 dB SNR data using the three methods. The red ones in (a) are the detection errors of the proposed method, the blue ones in (b) are the detection errors of the AIC method, and the yellow ones in (c) are the detection errors of STA/LTA method.

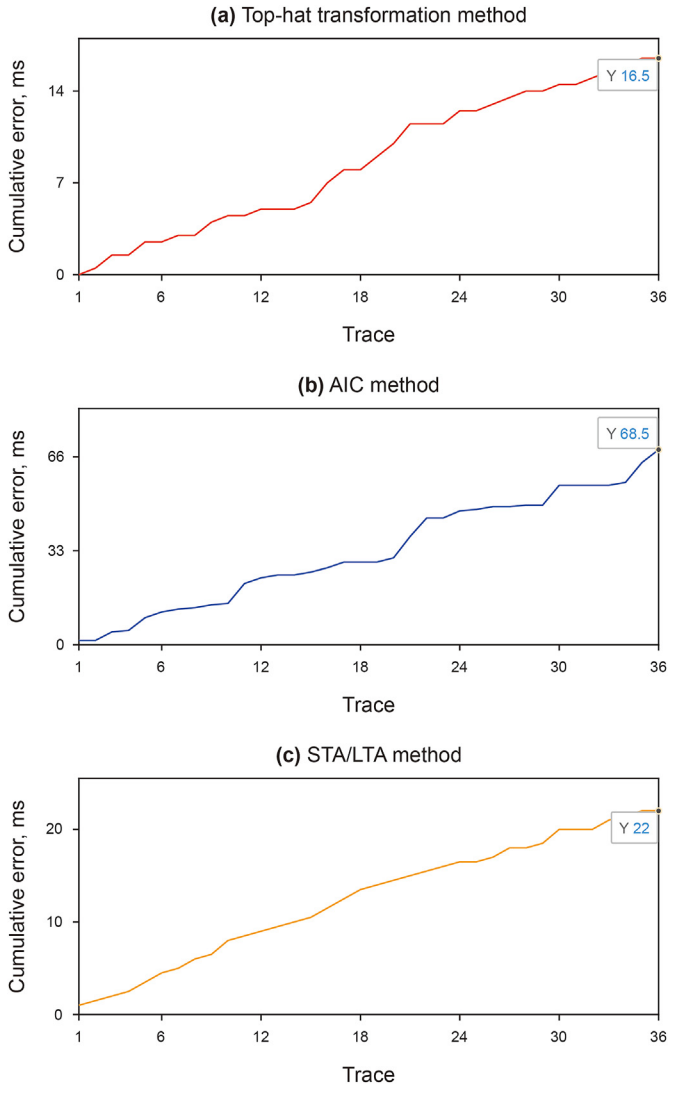


**Fig. 19.** The cumulative error of −1 dB SNR data using the three methods. The red ones in (a) are the cumulative errors of the proposed method, the blue ones in (b) are the cumulative errors of the AIC method, and the yellow ones in (c) are the cumulative errors of STA/LTA method. The number with Y label in the figure is the cumulative error in the last trace.

with the microseismic record, the position of the area where the maximum value of the selected section located is consistent with the peak area of the microseismic signal, the start point position is consistent with the position of the first break of the microseismic signal. The detection of microseismic signal can be achieved.

Next, the detection results of the proposed method are compared with other two method. Fig. 23 shows detection results of low SNR data by the three methods. It seems like the proposed method and STA/LTA method perform well, and it requires quantitative calculations to compare the performance of the three methods. Fig. 24 is the histogram of detection errors for the three methods calculated by Eq. (17). The errors of the three methods are obviously increased in the case of high SNR data, and the histogram shows that the proposed method performs better than the other two methods in terms of the maximum value of the detection error or the distribution law. Fig. 25 shows the cumulative errors of the three methods applied to low SNR data. The cumulative errors of the three methods are also significantly higher than those of the

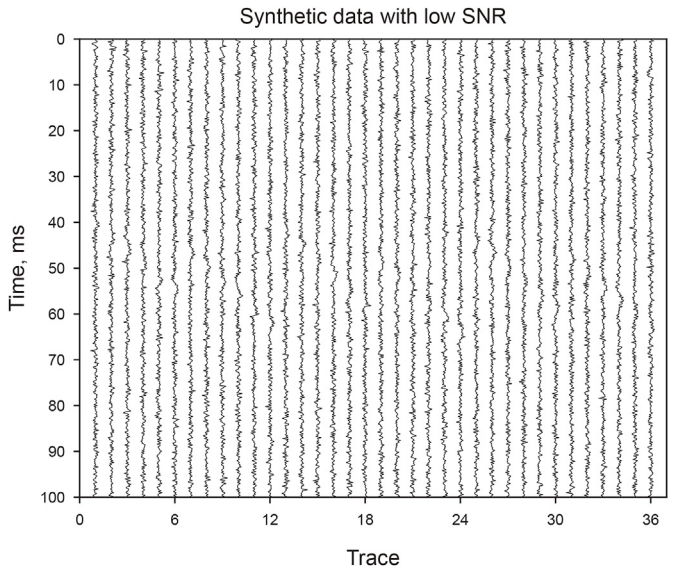


**Fig. 20.** Synthetic data with low SNR. The SNR is −13 dB.

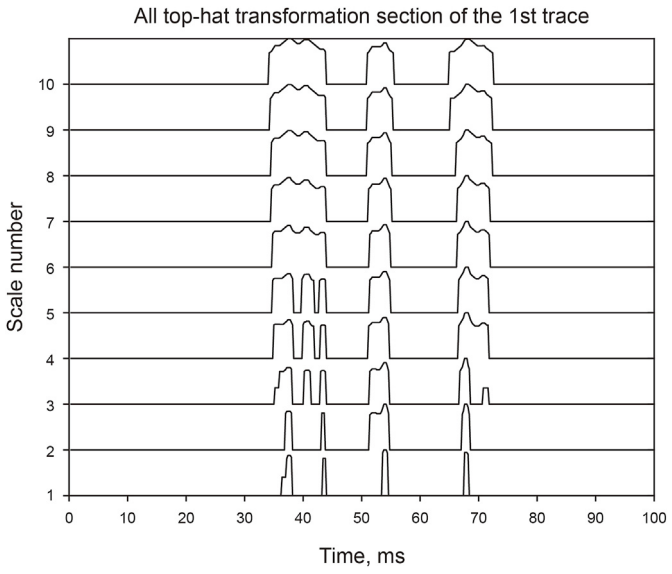


**Fig. 21.** All top-hat transformation sections of the first trace of −13 dB SNR data.

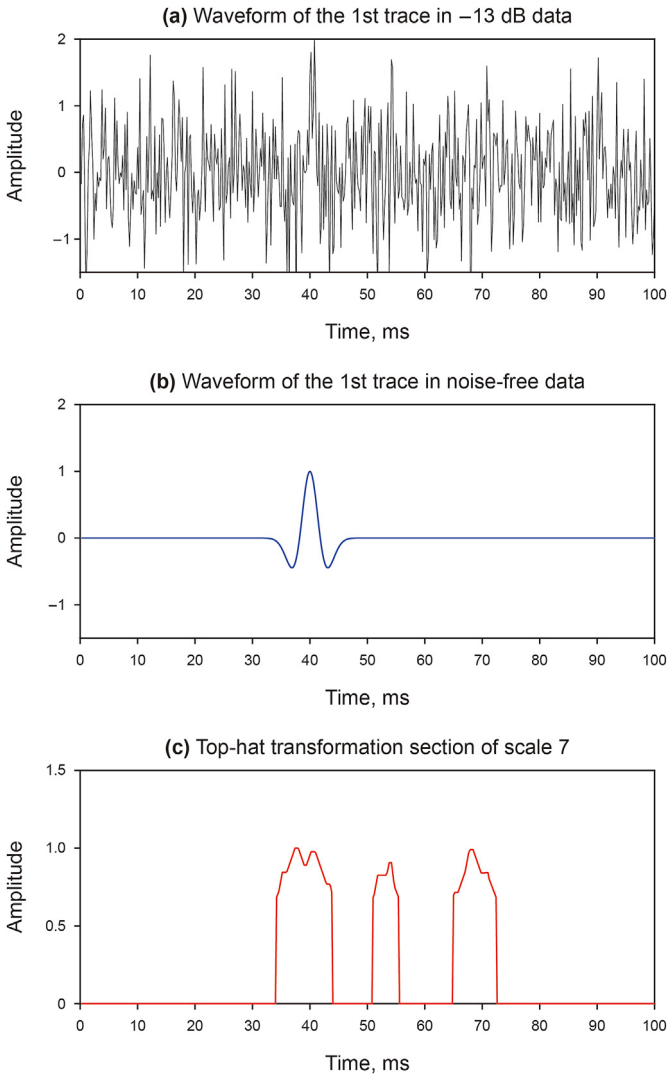


**Fig. 22.** Comparison of waveforms and selected scale section. The black waveform in (a) is the 1st trace in −13 dB data, the bule waveform in (b) is the 1st trace in noise-free data, and red waveform in (c) is the 7th scale section.

high SNR data. As the number with Y label shows, the proposed method has the smallest cumulative error which is not even half of the second smallest STA/LTA method. The proposed method greatly reduces the detection error in low SNR data. The proposed method has the best performance in microseismic events detection of the low SNR data.

### 3.3. Denoised low SNR synthetic dataset

In field microseismic data processing, the low SNR ratio data will be denoised, instead of weak signal detection directly on the low SNR data. In this section, the proposed method is tested in a low SNR synthetic data after filtering. The low SNR synthetic data is the data tested in previous section. As the dominant frequency is 50 Hz, a bandpass filter with 20–80 Hz is used, and the denoised waveforms are shown in Fig. 26. In the denoised data, the signal in most traces can be easily seen. However, just like the 11th trace, the signal in some traces is a smooth curve, and the signal are not

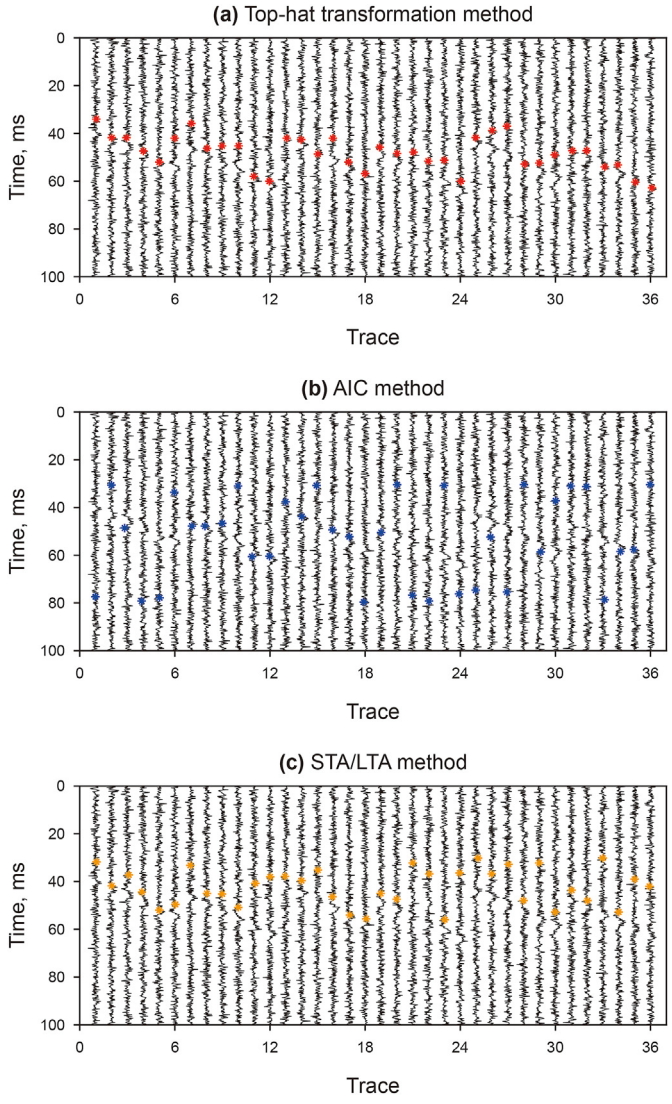


**Fig. 23.** The detection results of −13 dB SNR data using the three methods. The red ones in (a) are the detection results of the proposed method, the blue ones in (b) are the detection results of the AIC method, and the yellow ones in (c) are the detection results of STA/LTA method.

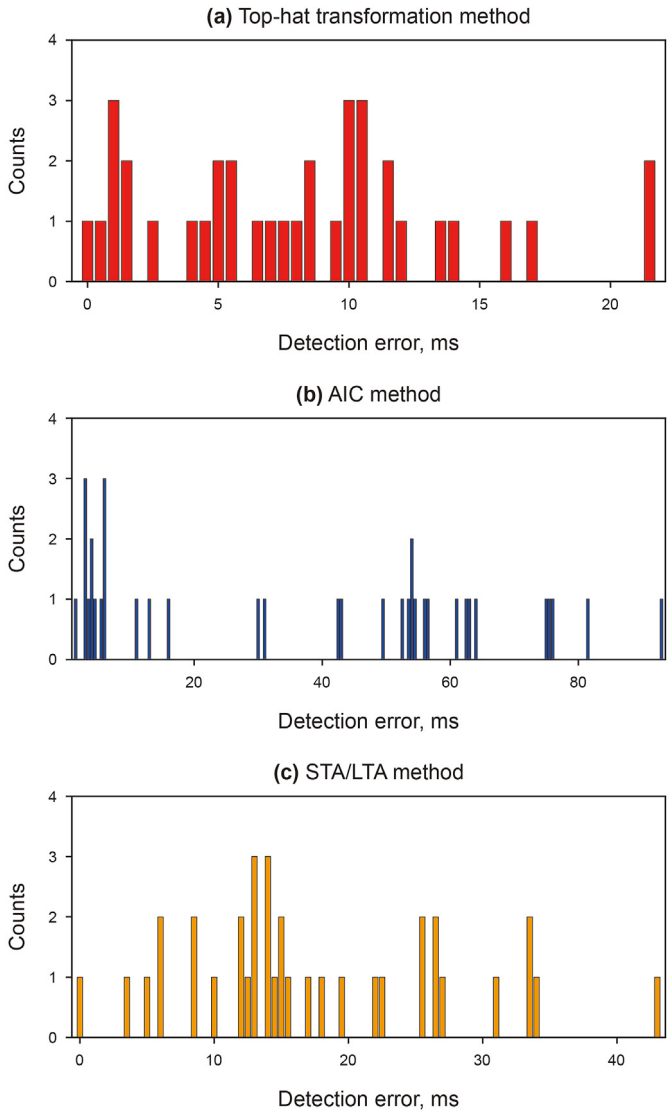


**Fig. 24.** The histogram of detection errors of −13 dB SNR data using the three methods. The red ones in (a) are the detection errors of the proposed method, the blue ones in (b) are the detection errors of the AIC method, the yellow ones in (c) are the detection errors of the STA/LTA method.

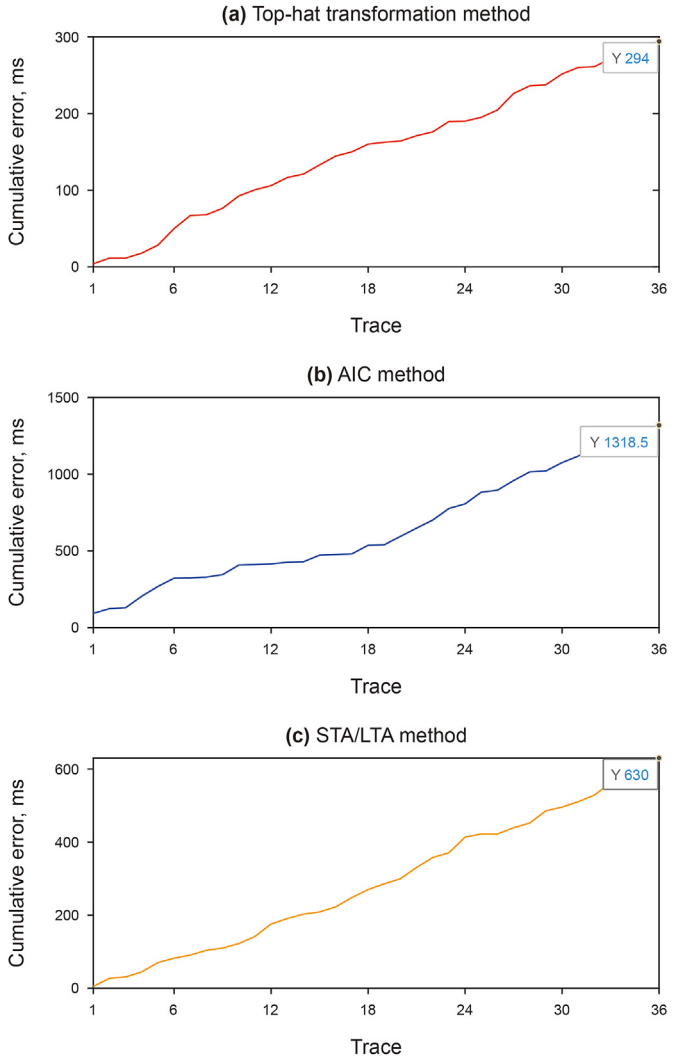


**Fig. 25.** The cumulative error of −13 dB SNR data using the three methods. The red ones in (a) are the cumulative errors of the proposed method, the blue ones in (b) are the cumulative errors of the AIC method, and the yellow ones in (c) are the cumulative errors of STA/LTA method. The number with Y label in the figure is the cumulative error in the last trace.

obvious. This is a challenge to the detection performance of the proposed method. Here again, the first trace record is selected as the template and the multiscale top-hat transformation section of this trace can be obtained. The length of initial SE is 9 and the total number of scales is 10 and the threshold is set to 0.15. The multiscale sections that after normalized are shown in Fig. 27. The scale sections after scale 7 have little change, and the 8th scale section is chosen for microseismic detection. Fig. 28 shows the waveform of 1st trace in both denoised and noise-free data and the selected 8th scale section. The waveform of this scale section has a great correlation with the microseismic record, the maximum position of scale section consistent with that of the microseismic signal, the start point position is consistent with the position of the first break of the microseismic signal. The detection of microseismic signal can be achieved.

Next, the detection results of the proposed method are compared with other two methods. Fig. 29 shows detection results of denoised low SNR data by the three methods. As for 11th trace,

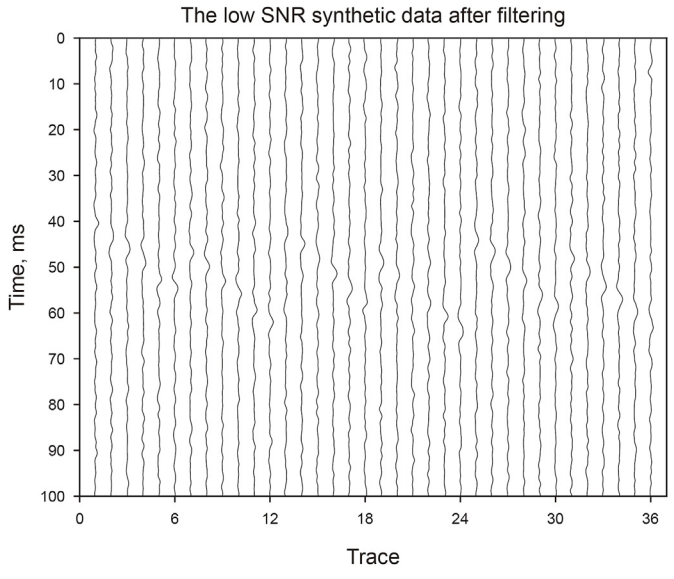


**Fig. 26.** The denoised waveform of the synthetic data with an original SNR of −13 dB.

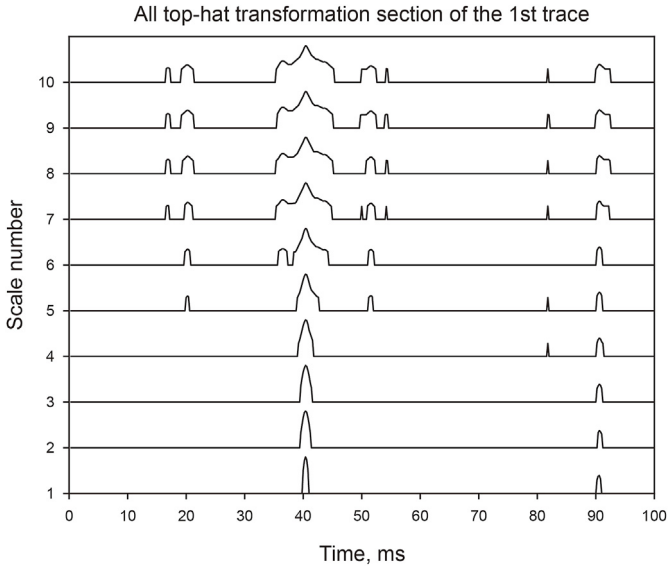


**Fig. 27.** All top-hat transformation sections of the 1st trace in denoised low SNR data.

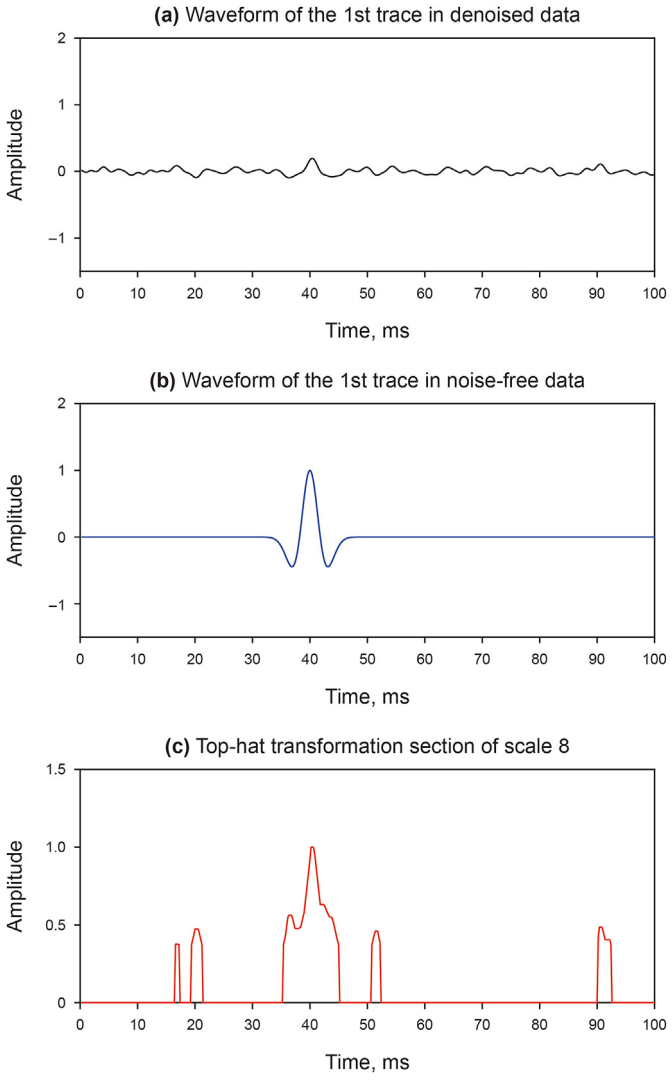


**Fig. 28.** The waveforms of original data and the selected scale section. The black waveform in (a) is the 1st trace, the red waveform in (c) is the 8th scale section.

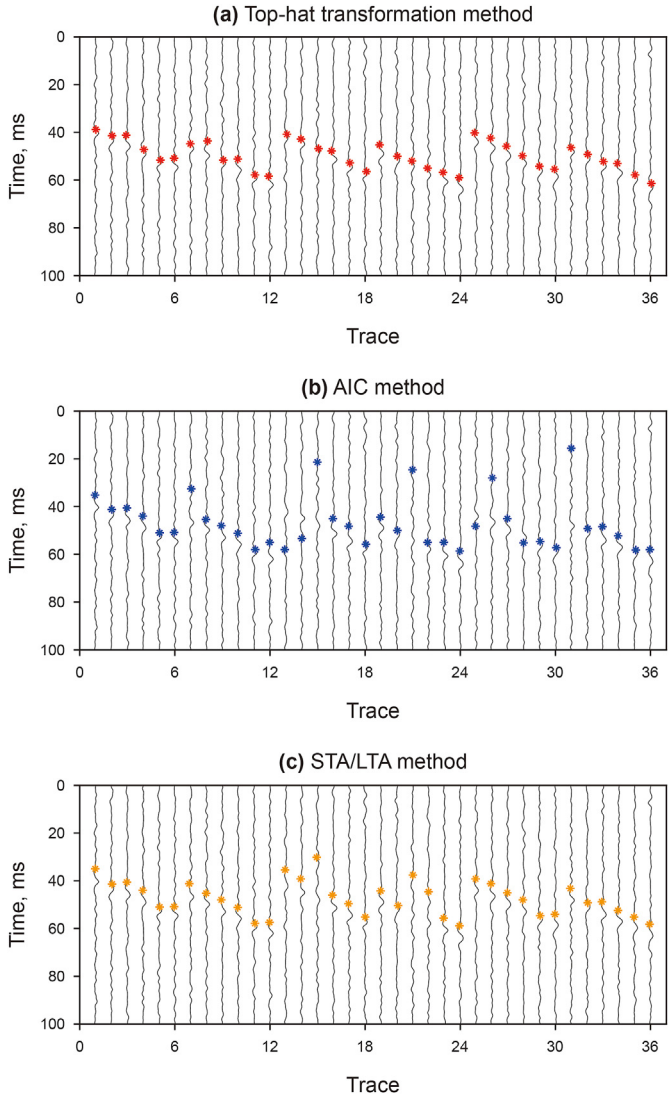


**Fig. 29.** The detection results of denoised data using the three methods. The red ones in (a) are the detection results of the proposed method, the blue ones in (b) are the detection results of the AIC method, and the yellow ones in (c) are the detection results of the STA/LTA method.

the first break detected by both AIC method and STA/LTA method greatly advanced, which is an obvious wrong result, while the first break detected by the proposed method is much more reasonable. Fig. 30 is the histogram of detection errors for the three methods calculated by Eq. (17). Overall, for the denoised low SNR data, the proposed method seems to have a well performance, which is also proved by the maximum value and distribution law of the identification errors in the histogram of the identification error. Fig. 31 shows the cumulative errors of the three methods applied to the denoised low SNR data. The cumulative errors of the three methods are significantly lower than those of low SNR data, but still higher than those of high SNR data. As the number with Y label shows, the proposed method has the smallest cumulative error, which is more than one third smaller than the second smallest STA/LTA method. The proposed method has the best performance in microseismic events detection of the denoised low SNR data.

## 4. Field dataset example

This section, the proposed method is applied to microseismic

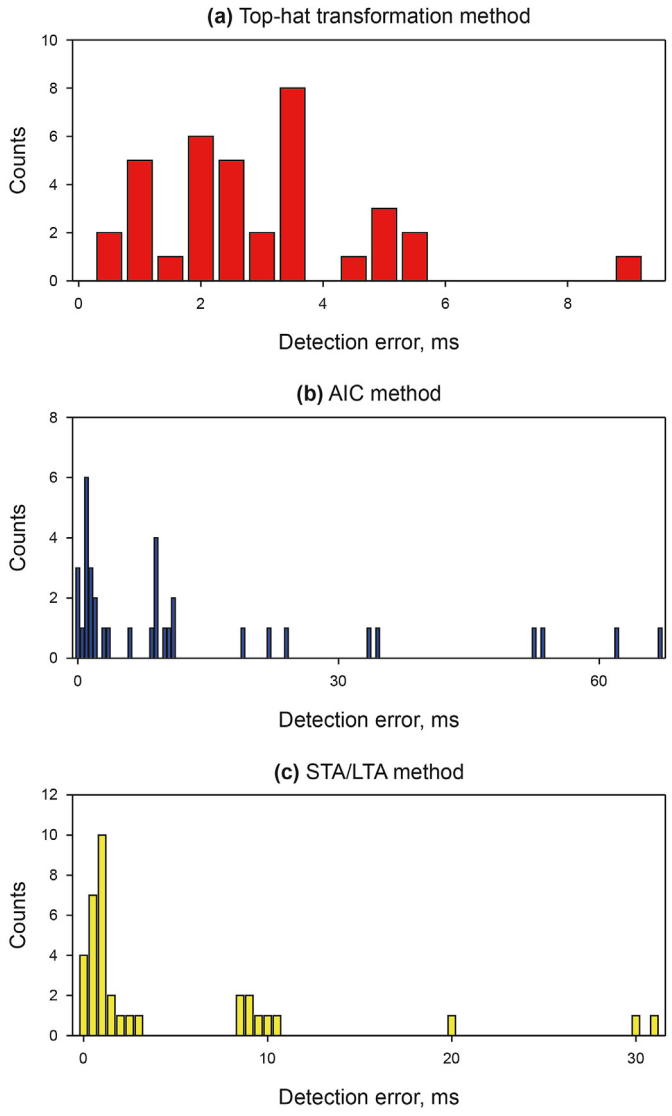


**Fig. 30.** The histogram of detection errors of denoised low SNR data using the three methods. The red ones in (a) are the detection errors of the proposed method, the blue ones in (b) are the detection errors of the AIC method, and the yellow ones in (c) are the detection errors of the STA/LTA method.

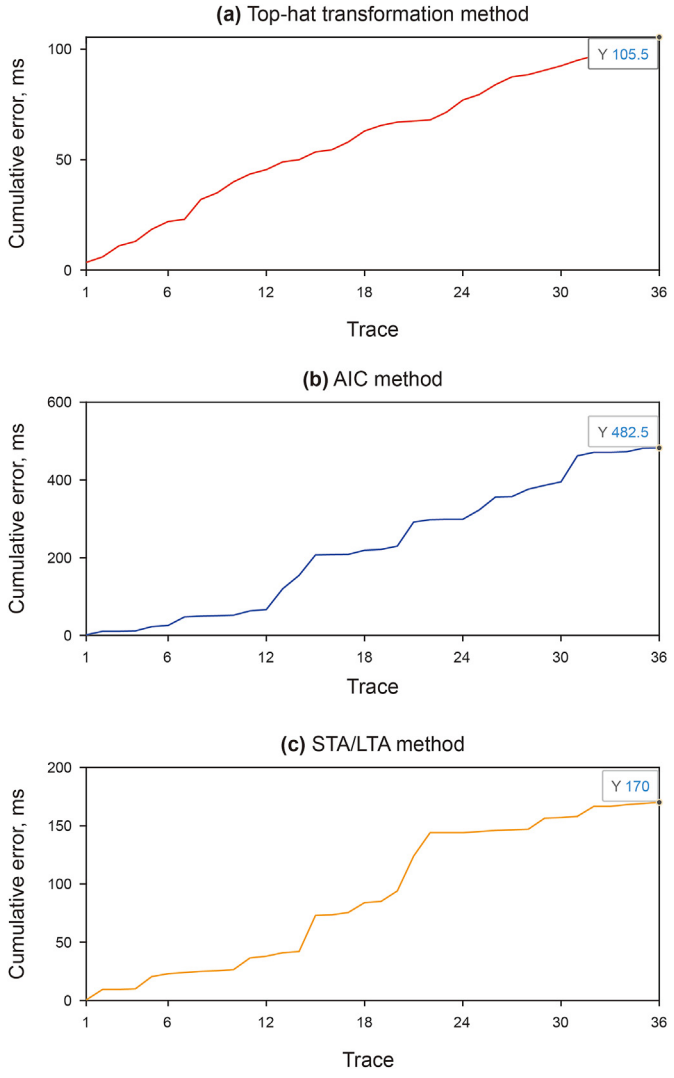


**Fig. 31.** The cumulative error of denoised low SNR data using the three methods. The red ones in (a) are the cumulative errors of the proposed method, the blue ones in (b) are the cumulative errors of the AIC method, and the yellow ones in (c) are the cumulative errors of STA/LTA method. The number with Y label in the figure is the cumulative error in the last trace.

data from a field microseismic monitoring project. The field data is a three-component microseismic record collected by in-well reception during hydraulic fracturing. The observation system is composed of 12 three-component geophones that vertically arranged in the monitoring well in almost a straight line, and the vertical distance between two adjacent geophones is 30 m. The time sampling interval of the microseismic records is 1 ms, and the length is 3008 sampling points. The waveforms of field data are shown in Fig. 32. The SNR of the X-components and Y-components are high, the microseismic signals are obvious, and have good coherence in the lateral direction. The SNR of some traces in the Z components are low, and it is difficult to detect signals.

In detection, the initial length of initial SE is 13, the total number of scales is 10 and the threshold is set to 0.5. Scale 7 sections were selected for signal detection. Fig. 33 shows the detection results of these three methods. It shows that except for the obvious errors of the 3rd and 26th detection results in the AIC method, the other detection results look reasonable. To compare the detection results of the three methods more precisely, the parts shown in the boxes

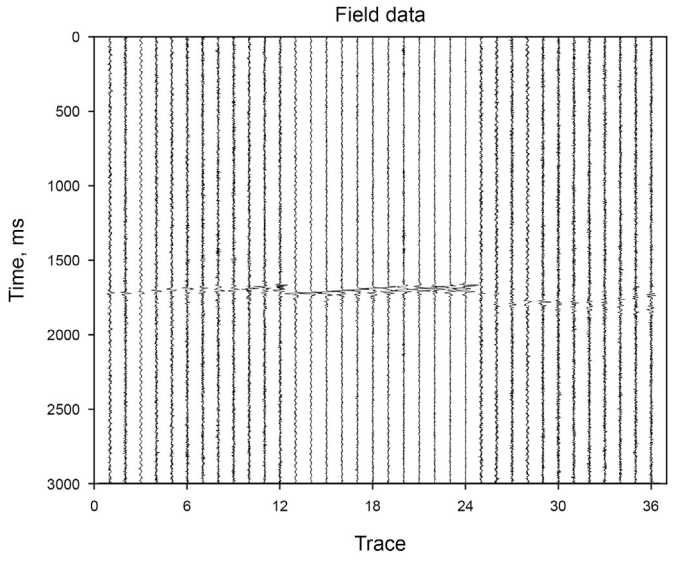


**Fig. 32.** The waveforms of field data. 1–12 traces are X components, 13–24 traces are Y components, and 25–36 traces are Z components.

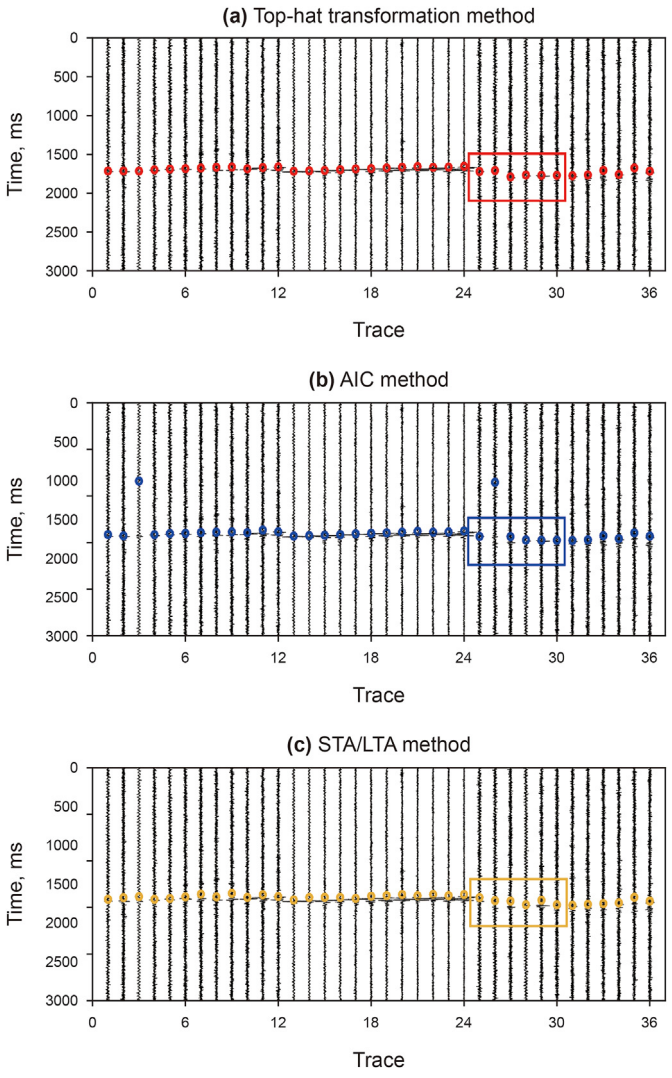


**Fig. 33.** The detection results of field data using the three methods. The red ones in (a) are the detection results of the proposed method, the blue ones in (b) are the detection results of the AIC method, and the yellow ones in (c) are the detection results of the STA/LTA method.

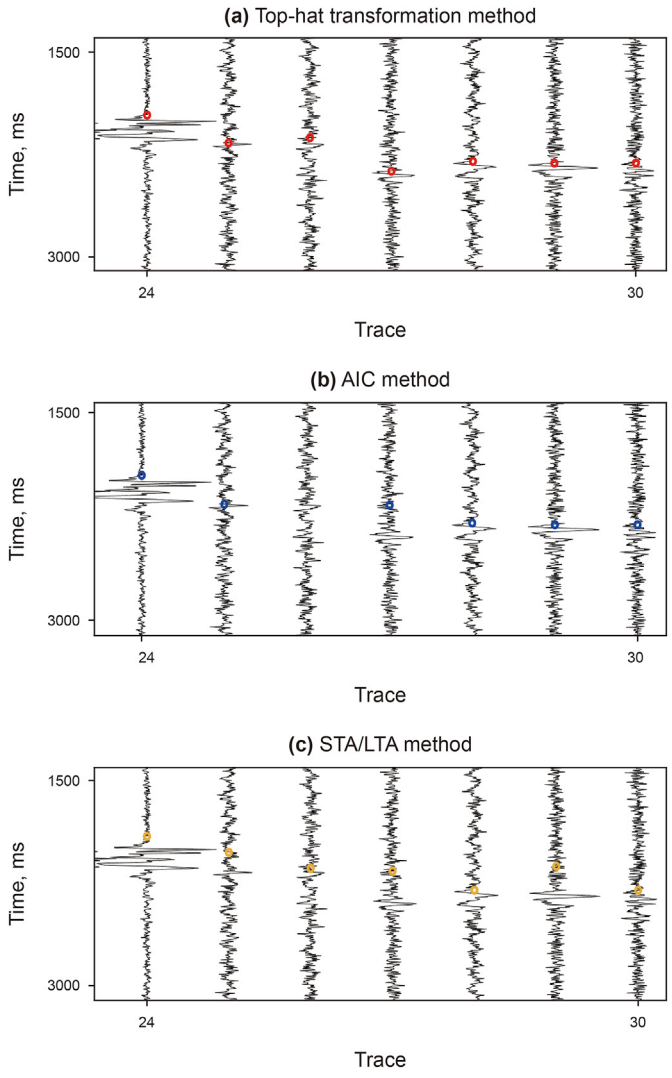


**Fig. 34.** The detection details of field data using the three methods. The red ones in (a) are the details of the proposed method, the blue ones in (b) are the details of AIC method, and the yellow ones in (c) are the details of the STA/LTA method.

in each picking result are enlarged respectively. Fig. 34 shows a zoomed-in detail of the detection results. Except for the obvious error of trace 26, the detection result of trace 27 of the AIC method is not the first break of the microseismic signal. As for the STA/LTA method, the detection results of traces 25, 27, and 29 are not the first breaks of microseismic signals, which are smaller than the exact first breaks. The proposed method does not have such problems. The details show that the proposed method has the best performance in effective signal detection of the field microseismic data.

## 5. Discussions

With the examples of synthetic data and field data, the top-hat transformation method demonstrates its advantages in detection of microseismic signal. This method is suitable for a variety of microseismic data with different SNR and has good noise immunity. Compared with the traditional STA/LTA method, as the method utilizes the waveform envelope characteristics of the microseismic signal, the detection result effectively avoids the drift of the first break point, with smaller error and higher accuracy.

On the other hand, this method is highly dependent on the key parameters such as the length of the initial SE, the number of scales, the scale selected for picking, and the threshold, especially the length of the initial SE and threshold. The error tolerance of these parameters is not high. It is very important to choose accurate parameters.

## 6. Conclusions

In this paper, a method is proposed for the automatic detection of microseismic events by multiscale top-hat transformation. In general, the method takes advantage of the difference between signal and noise in the different scale top-hat transformation section and achieves the detection of signal on a specific section. Firstly, based on the selected template trace, the appropriate type of SE, length of initial SE, number of scales and threshold are decided to get the multiscale top-hat transformation sections, then choose an appropriate scale section to achieve microseismic events detection. Finally, the detection of microseismic signals can be realized by applying these parameters to all the data. The method is

applied on both synthetic and field datasets, which achieves the accurately detection of microseismic signals. Compared with traditional methods, the proposed method has more obvious advantage both under low SNR conditions and when recorded as smooth curves. All the facts proved that the proposed method is an effective method for the automatic microseismic signal detection.

## Acknowledgments

This work was supported in part by the National Natural Science Foundation of China under Grant 41904098; and in part by the Fundamental Research Funds for the Central Universities, under Grant 2462018YJRC020 and Grant 2462020YXZZ006.

## References

Akram, J., Eaton, D.W., 2016. Refinement of arrival-time picks using a cross-correlation based workflow. J. Appl. Geophys. 135, 55–66. https://doi.org/10.1016/j.jappgeo.2016.09.024.

Albright, J.N., Pearson, C.F., 1982. Acoustic emissions as a tool for hydraulic fracture location: experience at the fenton hill hot dry rock site. Soc. Petrol. Eng. J. 22, 523–530. https://doi.org/10.2118/9509-PA, 04.

Allen, R., 1982. Automatic phase pickers: their present use and future prospects. Bull. Seismol. Soc. Am. 72 (6), S225–S242.

Baig, A., Urbancic, T., 2010. Microseismic moment tensors: a path to understanding frac growth. Lead. Edge 29 (3), 320–324. https://doi.org/10.1190/1.3353729.

Bai, X.Z., Li, Y., Zhou, F.G., 2012. Measure of image clarity using image features extracted by the multiscale top-hat transform. J. Opt. 14 (4), 045402. https://doi.org/10.1088/2040-8978/14/4/045402.

De Meersman, K., Kendall, J.M., van der Baan, M., 2009. The 1998 valhall microseismic data set: an integrated study of relocated sources, seismic multiplets, and s-wave splitting. Geophysics 74 (5), B183–B195. https://doi.org/10.1190/1.3205028.

Diehl, T., Deichmann, N., Kissling, E., et al., 2009. Automatic s-wave picker for local earthquake tomography. Bull. Seismol. Soc. Am. 99 (3), 1906–1920. https://doi.org/10.1785/0120080019.

Dong, J.N., Yuan, G.J., Wang, X.Y., et al., 2020. Experimental study of multi-timescale crack blunting in hydraulic fracture. Petrol. Sci. 18 (1), 234–244. https://doi.org/10.1007/s12182-020-00479-1.

Duan, Z.Y., Wang, R.Q., 2010. Application of multi-scale morphology in seismic data processing, 02 Explor. GeoPhys. Adv. 33, 135–140. +76. (in Chinese).

Gibbons, S.J., Ringdal, F., 2010. The detection of low magnitude seismic events using array-based waveform correlation. Geophys. J. Roy. Astron. Soc. 165 (1), 149–166. https://doi.org/10.1111/j.1365-246X.2006.02865.x.

Gou, X.T., Li, Z.M., Qin, N., et al., 2011. Adaptive picking of microseismic event arrival using a power spectrum envelope. Comput. Geosci. 37 (2), 158–164. https://doi.org/10.1016/j.cageo.2010.05.022.

Hafez, A.G., Rabie, M., Kohda, T., 2013. Seismic noise study for accurate P-wave arrival detection via MODWT. Comput. Geosci. 54, 148–159. https://doi.org/10.1016/j.cageo.2012.12.002.

Haralick, R.M., Sternberg, S.R., Zhuang, X., 1987. Image analysis using mathematical morphology. IEEE Trans. Pattern Anal. Mach. Intell. 9 (4), 532–550. https://doi.org/10.1109/TPAMI.1987.4767941.

Hu, T., Pang, X.Q., Jiang, F.J., et al., 2021. Key factors controlling shale oil enrichment in saline lacustrine rift basin: implications from two shale oil wells in Dongpu Depression, Bohai Bay Basin. Petrol. Sci. https://doi.org/10.1007/s12182-021-00564-z.

Huang, W.L., Wang, R.Q., Li, H.J., et al., 2017a. Unveiling the signals from extremely noisy microseismic data for high-resolution hydraulic fracturing monitoring. Sci. Rep. 7, 1–16. https://doi.org/10.1038/s41598-017-09711-2.

Huang, W.L., Wang, R.Q., Zhang, D., et al., 2017b. Mathematical morphological filtering for linear noise attenuation of seismic data. Geophysics 82 (6), V369–V384. https://doi.org/10.1190/GEO2016-0580.1.

Huang, W.L., 2019. Seismic signal recognition by unsupervised machine learning. Geophys. J. Int. 219 (2), 1163–1180. https://doi.org/10.1093/gji/ggz366.

Huang, W.L., Liu, J.X., 2020. Robust seismic image interpolation with mathematical morphological constraint. IEEE Trans. Image Process. 29, 819–829. https://doi.org/10.1109/TIP.2019.2936744.

Jiang, Y.Y., Wang, R.Q., Chen, X.Q., 2020. Automatic microseismic events detection using multiscale morphological characteristic function. IEEE Trans. Geosci. Rem. Sens. 58 (5), 3341–3351. https://doi.org/10.1109/TGRS.2019.2953676.

Kirbas, I., Peker, M., 2018. Signal detection based on empirical mode decomposition and Teager–Kaiser energy operator and its application to P and S wave arrival time detection in seismic signal analysis. Neural Comput. Appl. 28 (10), 3035–3045. https://doi.org/10.1007/s00521-016-2333-5.

Kuperkoch, L., Meier, T., Lee, J., et al., 2010. Automated determination of p-phase arrival times at regional and local distances using higher order statistics. Geophys. J. Int. 188 (2), 687–702. https://doi.org/10.1111/j.1365-246X.2010.04570.x.

Leonard, M., 2010. Comparison of manual and automatic onset time picking. Bull. Seismol. Soc. Am. 90 (6), 1384–1390. https://doi.org/10.1785/0120000026.

Li, H.J., Wang, R.Q., Cao, S.Y., et al., 2016. A method for low-frequency noise suppression based on mathematical morphology in microseismic monitoring. Geophysics 81 (3), V159–V167. https://doi.org/10.1190/GEO2015-0222.1.

Li, Q., Wang, R.Q., Huang, W.F., et al., 2005. Method for morphological filtering in seismic data processing. Petrol. Sci. 4, 20–29.

Li, X.N., Shen, J.S., Yang, W.Y., et al., 2019. Automatic fracture-vug identification and extraction from electric imaging logging data based on path morphology. Petrol. Sci. 16 (1), 58–76. https://doi.org/10.1007/s12182-018-0282-6.

Liu, H., Zhang, J.Z., 2014. STA/LTA algorithm analysis and improvement of Microseismic signal automatic detection. Prog. Geophys. 29 (4), 1708–1714. https://doi.org/10.6038/pg20140429 (in Chinese).

Liu, M.Z., Yang, J.X., Cao, Y.P., et al., 2017. A new method for arrival time determination of impact signal based on HHT and AIC. Mech. Syst. Signal Process. 86, 177–187. https://doi.org/10.1016/j.ymssp.2016.10.003.

Long, Y., Chen, J., Chen, Z.B., et al., 2020. Microseismic event automatic recognition method based on multi-traces envelope energy superposition technology. Prog. Geophys. 35 (4), 1424–1430, 10.6038/pg2020DD0350(in Chinese).

Matheron, G., 1975. Random sets and integral geometry. Wiley, New York.

Maxwell, S.C., Rutledge, J., Jones, R., et al., 2010. Petroleum reservoir characterization using downhole microseismic monitoring. Geophysics 75 (5), 129–137. https://doi.org/10.1190/1.3477966.

McCormack, M.D., Zaucha, D.E., Dushek, D.W., 1993. First-break refraction event picking and seismic data trace editing using neural networks. Geophysics 58 (1), 67–78. https://doi.org/10.1190/1.1443352.

Molyneux, J., Schmitt, D.R., 1999. First-break timing: arrival onset times by direct correlation. Geophysics 64 (5), 1492–1501. https://doi.org/10.1190/1.1444653.

Mousavi, S.M., Langston, C.A., 2016. Fast and novel microseismic detection using time-frequency analysis. SEG Tech. Progr. Expand. Abstr. 35, 2632–2636. https://doi.org/10.1190/segam2016-13262278.1.

Mousavi, S.M., Langston, C.A., Horton, S.P., 2016. Automatic microseismic denoising and onset detection using the synchrosqueezed continuous wavelet transform. Geophysics 81 (4), V341–V355. https://doi.org/10.1190/GEO2015-0598.1.

Mukhopadhyay, S., Chanda, B., 2000. Multiscale morphological approach to local contrast enhancement. Signal Process. 80 (4), 985. https://doi.org/10.1016/S0165-1684(99)00161-9, 696.

Mukhopadhyay, S., Chanda, B., 2001. Fusion of 2D grayscale images using multiscale morphology. Pattern Recogn. 34 (10), 1939–1949. https://doi.org/10.1016/S0031-3203(00)00123-0.

Mukhopadhyay, S., Chanda, B., 2002. An edge preserving noise smoothing technique using multiscale morphology. Signal Process. 82 (4), 527–544. https://doi.org/10.1016/S0165-1684(01)00143-8.

Muller, S., Legrand, J.F., Muller, J.D., et al., 1998. Seismic events discrimination by neuro-fuzzy-based data merging. Geophys. Res. Lett. 25 (18), 3449–3452. https://doi.org/10.1029/98GL52669.

Peng, B., Wang, Y., Yang, X.F., 2010. A multiscale morphological approach to local contrast enhancement for ultrasound images. In: 2010 International Conference on Computational and Information Sciences, pp. 1142–1145. https://doi.org/10.1109/ICCIS.2010.282.

Phillips, W.S., Fairbanks, T.D., Rutledge, J.T., et al., 1998. Induced microearthquake patterns and oil-producing fracture systems in the Austin chalk. Tectonophysics 289 (1–3), 153–169. https://doi.org/10.1016/S0040-1951(97)00313-2.

Provost, F., Hibert, C., Malet, J.P., 2017. Automatic classification of endogenous landslide seismicity using the random forest supervised classifier. Geophys. Res. Lett. 44, 113–120. https://doi.org/10.1002/2016GL070709.

Rouet-Leduc, B., Hulbert, C., Lubbers, N., et al., 2017. Machine learning predicts laboratory earthquakes. Geophys. Res. Lett. 44 (18), 9276–9282. https://doi.org/10.1002/2017GL074677.

Rutledge, J.T., Phillips, W.S., Mayerhofer, M.J., 2004. Faulting induced by forced fluid injection and fluid flow forced by faulting: an interpretation of hydraulic fracture microseismicity, Carthage Cotton Valley gas field, Texas. Bull. Seismol. Soc. Am. 94 (5), 1817–1830. https://doi.org/10.1785/012003257.

Saragiotis, C.D., Hadjileontiadis, L.J., Panas, S.M., 2002. PAI-S/K: a robust automatic seismic p phase arrival identification scheme. IEEE Trans. Geosci. Rem. Sens. 40 (6), 1395–1404. https://doi.org/10.1109/TGRS.2002.800438.

Serra, J., 1982. Image Analysis and Mathematical Morphology. Academic Press, New York.

Shahnas, M.H., Yuen, D.A., Pysklywec, R.N., 2018. Inverse problems in geodynamics using machine learning algorithms. J. Geophys. Res. Solid Earth 123 (1), 296–310. https://doi.org/10.1002/2017JB014846.

Shang, G.J., Shen, J.S., Huang, W.L., et al., 2019. Applying mathematical morphological top-hat transformation in seismic exploration for first break picking. 81st EAGE Conf. Exhib.Conference and Exhibition 1–5. https://doi.org/10.3997/2214-4609.201901384, 2019.

Shang, G.J., Shen, J.S., Huang, W.L., et al., 2020. Applying mathematical morphological top-hat transformation in microseismic first break picking. In: 2020 China Geosciences Joint Academic Annual Conference (in Chinese).

Tan, Y.Y., He, C., 2016. Improved methods for detection and arrival picking of microseismic events with low signal-to-noise ratios. Geophysics 81 (2), KS133–KS151. https://doi.org/10.1190/GEO2015-0213.1.

Trnkoczy, A., 2012. Understanding and parameter setting of STA/LTA trigger algorithm. In: Bormann, P. (Ed.), IASPEI New Manual of Seismological Observatory Practice 2. Deutsches Geo Forschungs Zentrum GFZ, Potsdam, pp. 1–20. https://doi.org/10.2312/GFZ.NMSOP-2_IS_8.1.

Vincent, L., 1993. Morphological grayscale reconstruction in image analysis: applications and efficient algorithms. IEEE Trans. Image Process. 2 (2), 176–201.

https://doi.org/10.1109/83.217222.
Wang, R.Q., Zheng, G.J., Fu, H.Z., et al., 2005. Noise-eliminated method by morphologic filtering in seismic data processing. +16-372 Oil Geophys. Prospect. 40 (3), 277–282. https://doi.org/10.13810/j.cnki.issn.1000-7210.2005.03.013 (in Chinese).
Wang, R.Q., Li, Q., Zhang, M., 2008. Application of multi-scaled morphology in denoising seismic data. Appl. Geophys. 5, 197–203. https://doi.org/10.1007/s11770-008-0033-3, 003.
Wang, Y.J., Li, H.L., Tuo, X.G., et al., 2020. Picking the P-phase first arrival of microseismic data with strong noise, 03 Geophys. Prospect. Pet. 59, 356–365 (in Chinese).
Yuan, S.Y., Zhao, Y., Xie, T., et al., 2022. SegNet-based first-break picking via seismic waveform classification directly from shot gathers with sparsely distributed traces. Petrol. Sci. 19 (1), 162–179. https://doi.org/10.1016/j.petsci.2021.10.010.
Yu, J.Q., Wang, R.Q., Liu, T.R., et al., 2014. Seismic energy dispersion compensation by multi-scale morphology. Petrol. Sci. 11 (3), 376–384. https://doi.org/10.1007/s12182-014-0351-4.
Yung, S.K., Ikelle, L.T., 1997. An example of seismic time picking by third order bicoherence. Geophysics 62 (6), 1947–1952. https://doi.org/10.1190/1.1444295.
Yu, Z.C., Tan, Y.Y., Zhai, S., et al., 2019. Arrival picking and global refinement for microseismic events based on waveform similarity. Chin. J. Geophys. 62 (12), 4782–4793. https://doi.org/10.6038/cjg2019M0296 (in Chinese).
Zhang, H.J., Clifford, T., Charlotte, R., 2003. Automatic p-wave arrival detection and picking with multiscale wavelet analysis for single-component recordings. Bull. Seismol. Soc. Am. 93 (5), 1904–1912. https://doi.org/10.1785/0120020241.
Zhang, J.J., Tang, Y.L., Li, H.J., 2017. STA/LTA fractal dimension algorithm of detecting the P-wave arrival. Bull. Seismol. Soc. Am. 108 (1), 230–237. https://doi.org/10.1785/0120170099.
Zhang, Y.L., Yu, Z.C., Hu, T.Y., et al., 2021. Multi-trace joint downhole microseismic phase detection and arrival picking method based on U-Net. Chin. J. Geophys. 64 (6), 2073–2085. https://doi.org/10.6038/cjg2021O0379 (in Chinese).
Zheng, G.J., Wang, R.Q., 2003. Application of mathematical morphology in seismic data processing. Prog. Explor. Geophys. 26 (4), 278–281 (in Chinese).
Zhou, C., Ju, X.G., Li, Z.A., et al., 2020. A deep convolutional generative adversarial network for first-arrival pickup from seismic data, 05 Geophys. Prospect. Pet. 59, 795–803. https://doi.org/10.3969/j.issn.1000-1441.2020.05.013 (in Chinese).